

Observation of early assembly events of Gag HIV-1

Ludwig-Maximilians-Universität München
Fakultät für Chemie und Pharmazie

Masterarbeit aus dem Fachgebiet

Physikalische Chemie

von

B.Sc. Bettina Motycka

geboren am 07.03.1994

in Wien

Beginn der Masterarbeit: 19.03.2018
Masterarbeit beim Prüfungsausschuss eingereicht am: 19.09.2018

Erklärung

Ich versichere, dass ich die vorgelegte Bachelorarbeit am Institut für Physikalische Chemie des Departements Chemie und Biochemie der Ludwig-Maximilians-Universität München im Arbeitskreis von Prof. Don. C. Lamb unter der Anregung und Anleitung von Dipl. Biochem. Philipp Messer selbstständig durchgeführt und keine anderen als die angegebenen Hilfsmittel und Quellen benutzt habe.

Freiwillige Einverständniserklärung:

Der Betreuer dieser Abschlussarbeit darf - unter der Angabe der Co-Autorenschaft des Verfassers der Masterarbeit - hieraus Daten verwenden und in wissenschaftlichen Zeitschriften veröffentlichen.

München, den 19.09.2018

(Bettina Motycka)

Erstgutachter: Prof. Don. C. Lamb
Zweitgutachter: Prof. Achim Hartschuh

Acknowledgment

First of all I want to thank Prof. D.C. Lamb for the opportunity to write my master thesis in his work group and for his constant encouragement and support. I would like to thank you again for taking me with to the meeting with the cooperation partners in Heidelberg.

Furthermore, I would like to thank Prof. A. Hartschuh for taking over the second expert opinion.

A special thank go to my supervisor Philipp, for his advice, the answer to all my questions, for the last minutes measurements and analyzes as well as for the correction of my thesis.

I would like to thank Evelyn, Adrian and Nader for their support and cheering me up when things didn't go so well.

I would also like to thank all members of FAB Lab for the nice welcoming, the awesome atmosphere in the group and for all the events. A special thank to the boulder group for the weekly workout.

Finally, I would like to thank my family and friends for their constant support, happy moments and the nice 2 years in Munich.

Contents

1	List of abbreviations	1
2	Introduction	2
3	Theoretical section	3
3.1	Gag polyprotein	3
3.2	Regulation of the PIP ₂ concentration at the PM	4
3.3	Virus development	5
3.4	Virus morphogenesis	6
4	Microscopy and spectroscopy techniques	9
4.1	Fluorescence	9
4.2	Fluorophores	10
4.2.1	Fluorescent proteins	11
4.2.2	Organic dyes	12
4.3	Total internal reflection fluorescence microscopy (TIRFM)	13
4.4	Fluorescence fluctuation spectroscopy (FFS)	15
4.4.1	Fluorescence Correlation Spectroscopy (FCS)	16
4.4.2	Image Correlation Spectroscopy (ICS)	16
4.4.3	Raster Image Correlation Spectroscopy (RICS)	17
4.4.4	Pulsed Interleaved Excitation (PIE)	20
4.5	Wavelet analysis	20
5	Experimental section	22
5.1	Cell preparation	22
5.1.1	Materials	22
5.1.2	Thawing	22
5.1.3	Splitting	23
5.1.4	Seeding for transfection	23
5.1.5	Transfection	23
5.1.6	Freezing	25
5.2	Methods	26
5.2.1	TIRFM	26
5.2.2	RICS	27
5.3	Analysis	29
5.3.1	Analysis of the TIRF data	29
5.3.2	Analysis of the RICS data	30
6	Results and discussion	32
6.1	Aim	32

6.2	Results of the TIRF measurements	32
6.2.1	Transfection optimization	32
6.2.2	Statistic of measured cells	33
6.2.3	Intensity traces	36
6.2.4	Assembly kinetics	38
6.2.5	Release of Gag clusters by addition of rCD1	41
6.3	Results of the RICS measurements	42
6.3.1	Diffusion coefficient	42
6.3.2	Cytosolic Gag concentration after cluster detachment via rCD1	45
7	Conclusion and outlook	48
	References	50
	List of figures	57
	List of tables	60
	Supplement	61

1 List of abbreviations

CA	capsid protein domain
CLSM	confocal laser scanning microscopy
D	diffusion coefficient
DNA	deoxyribonucleic acid
eGFP	enhanced green fluorescent protein
ESCRT	endosomal sorting complex required for transport
Env	viral envelope protein
FCS	fluorescence correlation spectroscopy
FFS	fluorescence fluctuation spectroscopy
FP	fluorescent proteins
G.E.U.	GFP aquivalent unit
HIV1	human immunodeficiency virus type 1
hpt	hours post transfection
IC	internal conversion
ICS	image correlation spectroscopy
ISC	intersystem crossing
IN	integrase
JF	Janelia Fluor Dye
MA	matrix protein domain
mRFP	monomeric red fluorescent protein
mRNA	messenger ribonucleic acid
NA	numerical aperture
NC	nucleocapsid domain
NHS	N-Hydroxysuccinimid
PIE	pulsed interleaved excitation
PI(4,5)P₂	phosphoinositide phosphatidylinositol 4,5-bisphosphate
PM	plasma membrane
PR	protease
PSF	point spread function
rCD1	reversible chemical dimerizer system
RICS	raster image correlation spectroscopy
RNA	ribonucleic acid
RT	room temperature
Rt	reverse transcriptase
TIRF	total internal reflection fluorescence
TIRFM	total internal reflection fluorescence microscopy
WF	wide field

2 Introduction

In the last decades the human immunodeficiency virus type 1 (HIV-1) became an increasingly scientific topic. The HIV-1 virus belongs to the group of retroviruses. During infection, the virus proteins enter the host cell through binding to cellular receptors followed by a fusion of the virus membrane with the outer cell membrane. During the fusion the viral genetic material is transferred into the cell. The virus RNA is then transcribed into DNA by reverse transcriptase in the cytosol. Afterwards this DNA is subsequently integrated into the genome of the host cell by a retroviral integrase. As soon as the genetic material, the DNA, of the virus is expressed, morphogenesis occurs, starting in the cytoplasm. ^{[1][2]}

The virus development from its building blocks into a mature and infectious form can be divided into three stages. The first step where the virus proteins in the cytoplasm anchor to the plasma membrane (PM) of the host cell is called assembly, clustering and bulging of the membrane. The second stage is known as budding, where the fission from the host cell occurs. As third step maturation occurs, but it is still unknown when exactly. It could be after budding but it could be during budding, too.^[1] Whereas this step, the immature virus is transformed into its mature and infectious form. This is mediated by structural changes through cleavage of the Gag and the Gag-Pro-Pol polyprotein at ten different sites by protease enzymes.^[1]

The coordination of all these steps is carried out by the Gag polyprotein. This protein is the major structural protein of HIV-1, which makes it an interesting target for research. Additionally, the genomic RNA-binding site is also localized on this protein. As already mentioned, it is known that the morphogenesis can be divided into three stages, but how the molecular mechanism works in detail is still unknown.

In this respect, the focus of my master thesis is primarily set on the viral assembly, or more precisely on how the assembly process at the PM works in detail. One important question which has to be answered in this respect is when the Gag anchors to the PM and at which period of time this clusters are formed. Main question was whether the Gag bind to the membrane as monomers or oligomers during the assembly step and whether the oligomerization happens directly at the membrane or earlier in the cytosol.

The most promising method to study the kinetics of the virus assembly in live cells are fluorescence-based methods. In this work total internal reflection fluorescence microscopy (TIRM) and raster image correlation spectroscopy (RICS) were used to address this issues.

3 Theoretical section

3.1 Gag polyprotein

Gag is with about 50% of the entire virion mass the main constituent and major structural protein of HIV-1. Gag and its frameshift variant, Gag-Pro-Pol, mediates and coordinates the important processes which occurs during the virus morphogenesis: assembly, budding and maturation.^[4]

Gag is essential for the anchoring of the virus particles to the PM, for the creation of spherical particles by mediating protein-protein interactions and also the binding site for the genomic RNA is localized at the Gag polyprotein. All these morphogenic processes seem to take place simultaneously at the PM of the living host cell. This makes Gag to the most important component of the HIV-1.

The protein consists of four major subdomains and two spacer peptides (see **Figure 1**).^[1] The amino-terminal end of the Gag polyprotein (MA) is required for the binding to the PM as well as for the recruitment of the viral envelope proteins (Env).^[1] The capsid protein domain (CA) mediates the protein-protein interactions, which are primarily important for the assembly of immature virion particles and subsequently for the creation of the conical capsid in the mature virus.^[1] Two copies of the viral zinc-finger motive are located at the Gag nucleocapsid domain (NC) and function there as a binding site for the viral genome and other nucleic acid during the assembly. The carboxyl-terminus end of Gag p6 is a multi-purpose binding site for several other proteins, including accessory viral proteins.^[1]
[5]



Figure 1: Schematic representation of Gag. The protein consists of four domains, the matrix domain (MA), the capsid domain (CA), a nucleocapsid domain (NC) and a P6 domain as well as the two spacer peptides SP1 and SP2 and . The cleavage sites are shown in black arrows.^[1]

Besides these domains, Gag also harbours two spacer peptides, SP1 and SP2, which play a crucial role during the viral maturation by regulating the configurational changes.^[1] All subdomains are separated through flexible linker regions, which all contain a protease cleavage site. During maturation the viral protease separates the Gag domains by cutting the polyprotein at these linker regions.^[1]

Further analysis showed that the N-terminal myristoyl moiety of Gag together with the basic residuals at the surface of the MA domain are essential for Gag targeting and anchoring to the PM.^{[15] [16][17]} Upon arrival of Gag at the PM it interacts with the plasma membrane specific lipid phosphatidylinositol-(4,5)-bisphosphate (PI(4,5)P₂) or shorter PIP₂.^{[2][3]} This leads to an outward flip of the 2'-acyl chain of the PIP₂, followed by the displacement of the myristate from the acyl binding pocket of the MA domain. The myristate moiety in turn would insert into the PM. A consequent exchange of the unsaturated 2'-acyl chain of PIP₂ by the saturated myristic acid occurs. This configurational myristoyl switch allows Gag to bind to the inner leaflet of the PM (**Figure 2**). Depletion of PIP₂ causes a loss of binding activity of Gag to the PM, while increasing concentration at the intracellular membrane leads to a stable Gag anchoring.^{[2][14] [18] [21]}

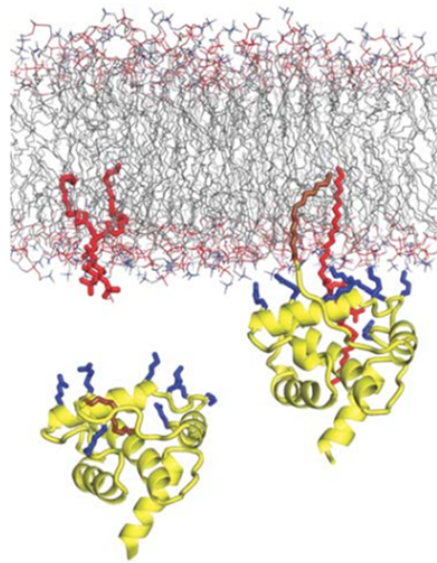


Figure 2: Gag MA domain (yellow) anchoring to the inner leaflet of the PM (gray) via myristoyl switch. The aliphatic myristoyl group (brown) and the basic residues on the membrane binding surface of the MA surface (blue) interact with the PIP₂ (red).^[18]

Recent advances in lipid mass spectroscopy have allowed to study the viral lipid composition of infected HIV-1 cells. The results revealed that beside the high level of PIP₂ there is a strong enrichment of the so called "raft lipids", include sphingomyelin, cholesterol and plasmalogen phosphatidyl ethanol. This enrichment causes an increase in saturated fatty acids compared with the producer cell membrane.^{[19] [20]}

3.2 Regulation of the PIP₂ concentration at the PM

The attachment of Gag to the PM of infected cells occurs stochastically and depends on the myristoylated MA domain of the Gag and the concentration of PIP₂. After anchoring of Gag to the PM, the concentration of PIP₂ is still important for the Gag targeting because

PIP₂ controls the localization of cellular proteins at the PM. To study PIP₂-dependent efficiency of the targeting and anchoring of the Gag during assembly, a novel chemical biological tool, developed by researchers of the University Hospital Heidelberg, Germany, was used. [2]

The principle behind the reversible chemical dimerizer system (rCDS) is illustrated in **Figure 3**. The translocation of the anchor phosphatase by rCD1 is the cause of the recruitment to the PM of the phosphatase. This leads to a reduction of the PIP₂ level by converting to PIP through dephosphorylation. As a result, Gag that already bound to the PM detaches again. FK506, the competing ligand of rCD1, which binds better than rCD1, leads to a displacement of the enzyme from the PM into the cytosol. As a result the PIP₂ concentration at the inner leaflet of the PM is restored rapidly. [2]

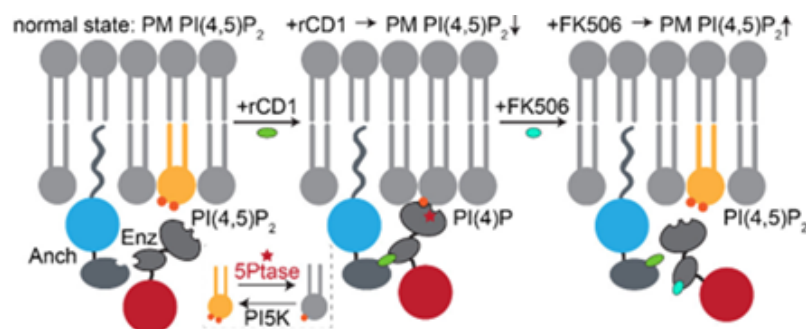


Figure 3: Schematic illustration of the principle of the reversible chemical dimerizer system for controlling PIP₂ concentration. The anchor is shown in blue and in red the enzyme phosphatase localized at the inner leaflet of the PM. Under normal PIP₂ concentration the Gag can bind to the inner leaflet of the PM, by adding rCD1 (green) the concentration of phosphatase at the PM increases, which causes a conversion from PIP₂ to PIP. No Gag can bind to the PM unless FK506 (blue) is added. This causes the displacement of the enzyme from the PM, which restores PIP₂ levels rapidly. [2]

3.3 Virus development

First of all, the proviral DNA is integrated into the host chromosome shown in **Figure 4**. The genomic RNA, where all virals proteins are encoded on, serves as messenger RNA (mRNA) for Gag and Gag-Pro-Pol. After transcription it is important that the viral mRNA is correctly spliced, polyadenylated and capped, so that it can leave the nucleus of the host cell over the endogenous mRNA export route the promote the coordinate synthesis of Gag and Gag-Pro-Pol in the cytosol. Alternatively the export of the RNA out of the nucleus occurs over the Rev-dependent export pathway. [1]

An assembled virion consists beside the Gag shell of two copies of the positive sense genomic viral RNA and cellular t-RNA molecules, which are used to prime the cDNA synthesis. [9] The dimerization of the genomic RNA takes place in the cytosol and is not

only essential for building the RNA-Gag polyprotein complex but also for viral infectivity. During this process the replicated RNA is recognized by cis-acting sequences localized at the NC-domain of Gag.^[10]

Additionally to the RNAs there are three viral enzymes, on the one hand protease (PR) as part of the Gag and on the other hand reverse transcriptase (Rt) and integrase (IN), which are packaged to the Gag.^[1] The enzymes as parts of the Gag ensure that all bounded components have the correct stoichiometry.^[11] This makes it possible for other viral components to bind via protein-RNA or protein-protein interaction to the Gag polyprotein. The Gag with all important components bound arrives at the PM of the host cell, where the virus morphogenesis starts.

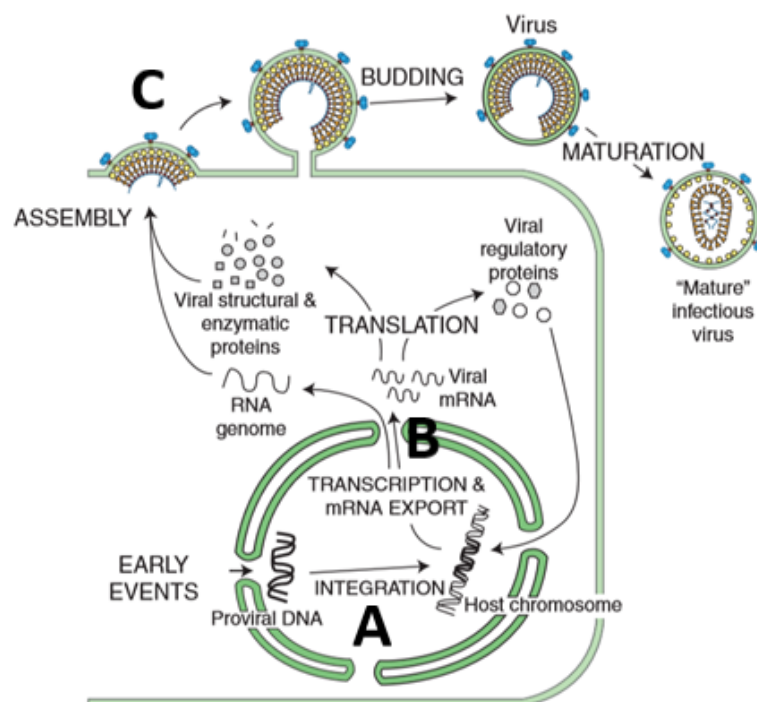


Figure 4: Development of the HIV-1, from infection to maturation. In (A) the integration of the proviral DNA into the host chromosome occurs followed by (B) the transcription and transport of the mRNA out of the nucleus and finally (C) the virus morphogenesis takes place.^[1]

3.4 Virus morphogenesis

As it was previously stated, the morphogenesis of the virus can be separated in three stages: assembly, budding and maturation (**Figure 5**).

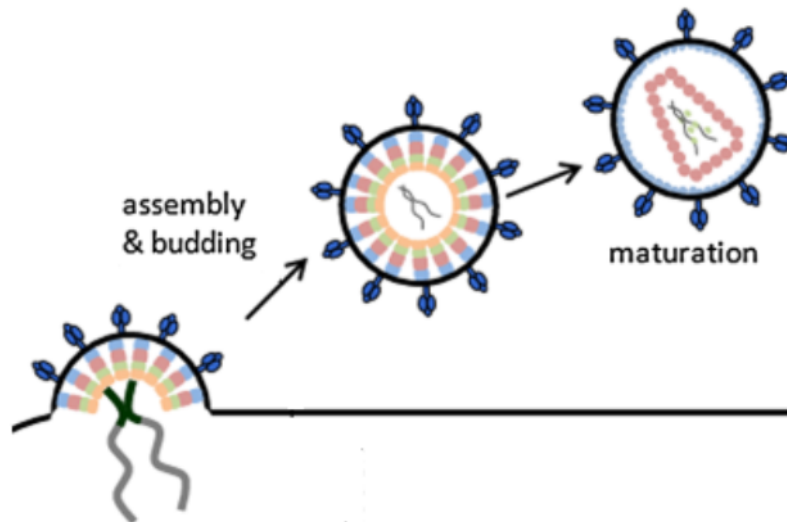


Figure 5: Illustration of the three stages of virion development. The viral genetic material is depicted in green-gray, Gag in colored blocks and the envelope glycoprotein in blue.^[3]

Researchers found out that Gag and their proteolytic maturation products usually arrive as monomers or dimers at the PM.^[2] In most cases the attached Gag is not polymerized extensively before reaching the membrane.^[7] It is still unknown if the polymerization of Gag takes place at the nucleation sites at the PM composed by Gag-RNA complexes or earlier in the cytoplasm.^{[7][8]}

After the assembly and anchoring of Gag to the PM as spherical immature particles budding starts. The budding is mediated by the endosomal sorting complex required for transport (ESCRT) machinery, a sophisticated mechanism normally involved in endosomal sorting and cytokinesis.^[23] Without the ESCRT factors, the virus morphology typically arrests in a late state of the virus assembly in which the whole Gag shell is connected to the PM through a thin membrane “stalk”. This means that the ESCRT pathway mediates the membrane fusion and virion release if all necessary components are present. ^[33]

ESCRT consists of 4 heteromeric complexes promoting different kinds of membrane processes.^[25] It is recently emerged that subunits of ECSRT proteins, appear to form inward spiraling filaments within the neck of the budding virus.^[26] This inward spiraling domains create closed “domes” which constrict the opposing membranes and promote the fission of the enveloped viruses out of the host cell.^{[24][27]}

The viral maturation, a dynamic and multi step process, begins concomitant with budding or immediately followed. During this process, the viral dimeric aspartic enzyme protease is activated through dimerization and cleaves Gag by recognizing five specific cleavage sites into its different components.^[28] This causes a dramatically rearrangement of the proteins to create the mature and infectious virus, with its characteristic conical core.^{[1][30]}

This core has a geometric structure, which consist of hexagonal nets to enclose the entire viral RNA.^{[31][32]}

4 Microscopy and spectroscopy techniques

In the last years, researchers used electron microscopy and electron tomography to receive information about virion composition and architecture, as well as the localization of Gag-Gag interaction and their functional role.^{[34][35]} Although those methods have yielded great information about the HIV-1 processes, the kinetics behind these events were still unknown, because of the fixated state of the particles. One big problem of those methods is that they only display still images and not well suited for larger number of individual particles with different movements.^[36]

The interest in observing the processes inside of living-cells has been increased in the past. One big challenge is that biochemical studies are limited by the fact that the assembly, release and maturation steps occur stochastically. To bypass these problem, one promising method is to label specific components of the cell with fluorophores and measuring afterwards their fluorescence with sensitive fluorescence microscopic techniques. These fluorescence-based methods, such as TIRM or RICS, are excellent methods to visualize the individual aspects of virus cell interaction, for example the HIV-1 assembly, and the dynamics of this process.^[36]

4.1 Fluorescence

Light, which can either be seen as an electromagnetic wave or as a particle, called photon, can interact with matter. Matter is made up of charged particles, composed of a positively charged nucleus surrounded by electrons. There are several ways that light can interact with matter (**Figure 6**).^[37]

The total energy of a molecule is depended on the its electronic, vibrational, rotational and translation energy. At room temperature the molecule will be in its electronic ground state (S_0) of a harmonic potential well. The absorption of photons leads to an energization of the molecule, whose shell electrons are thus excited from the ground state to the excited state (S_1 or S_2). This electronic excitation in the molecule only occurs if the energy difference between the two states is equivalent to the energy of the photon. The most favorable transitions are those between states where it comes to an overlapping of the electronic state. The grater the overlap between the vibrational states the higher is the transition probability, also known as Franck-Condon principle.^[37]

If the energy of the absorbed photon is high enough, it could force a molecule in the S_2 state to relax to the ground state. During this process, which is known as stimulated emission, a photon is emitted.^[37]

In contrast to the stimulated emission, fluorescence occurs spontaneously in the range of nanoseconds. Fluorescence, or spontaneous emission, is the probability of an excited electron to drop spontaneously from the S_1 to the S_0 by emission of a photon.^[38]

An electron transition from an excited singlet to an excited triplet state, an energy state of higher spin multiplicity, is established as intersystem crossing (ISC). If only spin forbidden transitions are available to return to the lower energy singlet state, the excited electron can be trapped in the triplet state. This process is called phosphorescence, where it takes longer for the molecule to fall back from the excited state to the ground state compared to fluorescence.^[38]

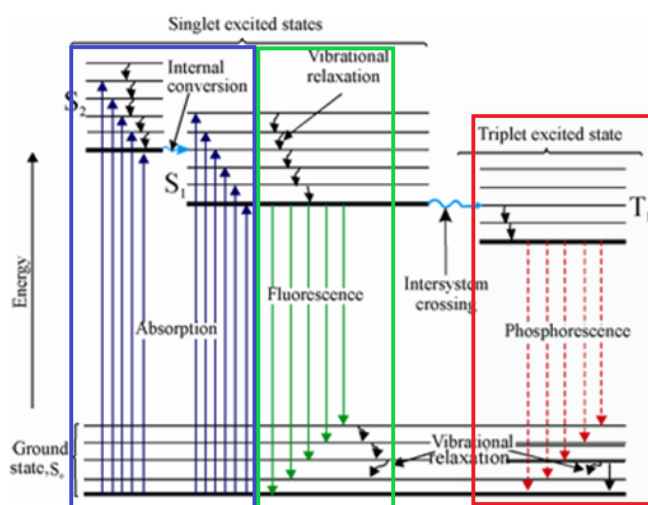


Figure 6: Jablonski diagram, which shows possible energy transitions and mechanism. In blue the absorption of an electron from the energetic ground state (S_0) to the excited state (S_1 or S_2) is presented. Green illustrates the fluorescence mechanism and in red the phosphorescence is pictured.^[39]

4.2 Fluorophores

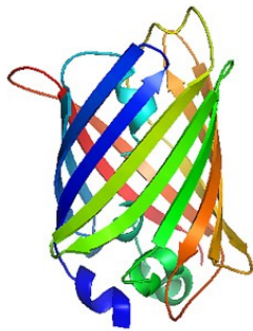
To measure single molecule fluorescence it is necessary to label the molecules of interest with fluorophores. There are three common used types of fluorophores: organic fluorophores, fluorescent proteins and nanocrystals (aka Quantum dots). The properties of the particular fluorophores are strongly dependent on the molecular environment. As an example, photobleaching, the irreversible decomposition of the fluorescent molecules via the excited triplet state, can appear. This is caused by interactions with for example molecular oxygen or other oxidative molecules before the emission occurs.

To observe virus assembly within living cells, it requires the attachment of a suitable fluorophore to a viral component. It has been shown that the Gag as structural component

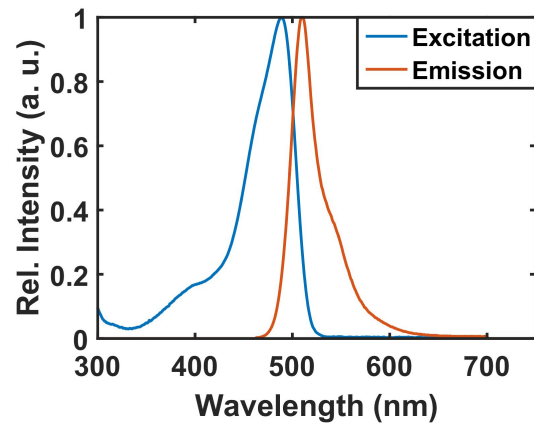
is the most abundant one. This fact renders it as an attractive target for labeling. The mostly used strategy is the use of fluorescent proteins (FPs), such as eGFP and mRFP, or organic dyes. [40]

4.2.1 Fluorescent proteins

The enhanced green fluorescent protein (eGFP) is a genetically engineered variation of a natural occurring FP from the jellyfish *Aequorea Victoria* and was discovered in 1961. It consists of 238 amino acid residues and the enhanced type is 35 times brighter than the wild-type.[41] The protein has a green fluorescence when exposed to light in the blue to green range. The excitation maximum is at a wavelength of 488 nm and the emission maximum at 507 nm (**Figure 7**).[41]



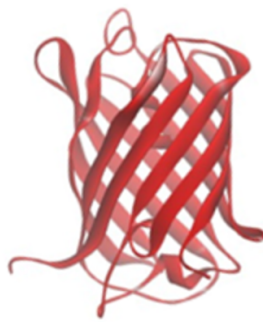
(A)



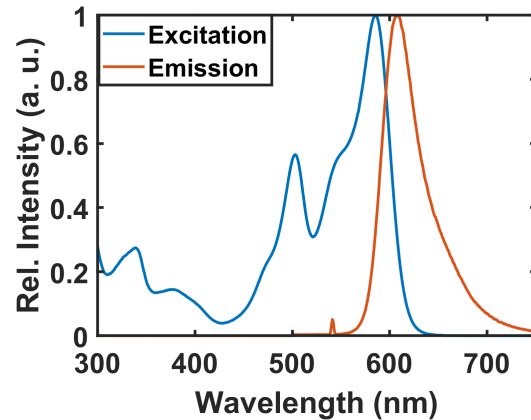
(B)

Figure 7: (A) Crystal structure of the green fluorescent protein and (B) the spectra of the excitation (blue) and emission (red). [41]

The monomeric red fluorescent protein (mRFP) is derived from *Discosoma sp.*, and has a size of approximately 236 amino acids. In **Figure 8** it can be seen that this protein has the excitation peak at 558 nm and the emission maximum occurs at a wavelength of 583 nm. [42]



(A)



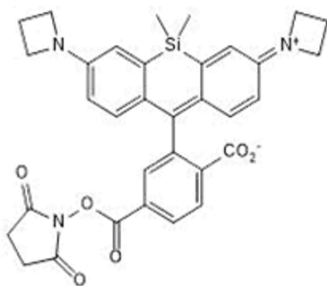
(B)

Figure 8: (A) Crystal structure and (B) the excitation (blue) and emission (red) spectra of a monomeric red fluorescent protein.^[43]

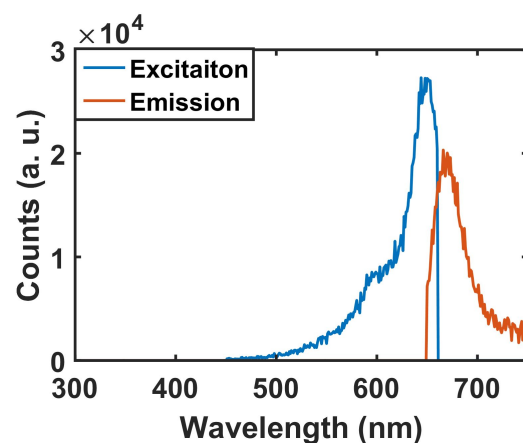
4.2.2 Organic dyes

Organic dyes are water soluble and their photophysics are well characterized. A big advantage in comparison to FP is their high photostability, which makes them a common method for targeting. However, for cell experiments a system, for example CLIP, is needed to bind the dye to the molecule.

JF646, a red fluorescence dye, is supplied for coupling to primary amine groups (**Figure 9**). By means of the spectra it can be seen that the excitation maximum is at 646 nm and the emission maximum at 664 nm. ^[44]



(A)



(B)

Figure 9: (A) The structure and (B) the excitation emission spectra of the red fluorescence dye JF646 as NHS-coupled derivative.^[44]

A yellow fluorescence dye (JF549) is commonly used as an NHS ester for coupling to primary amine groups. The excitation peak of the dye is at a wavelength of 549 nm and the emission peak at 571 nm (**Figure 10**).^[44]

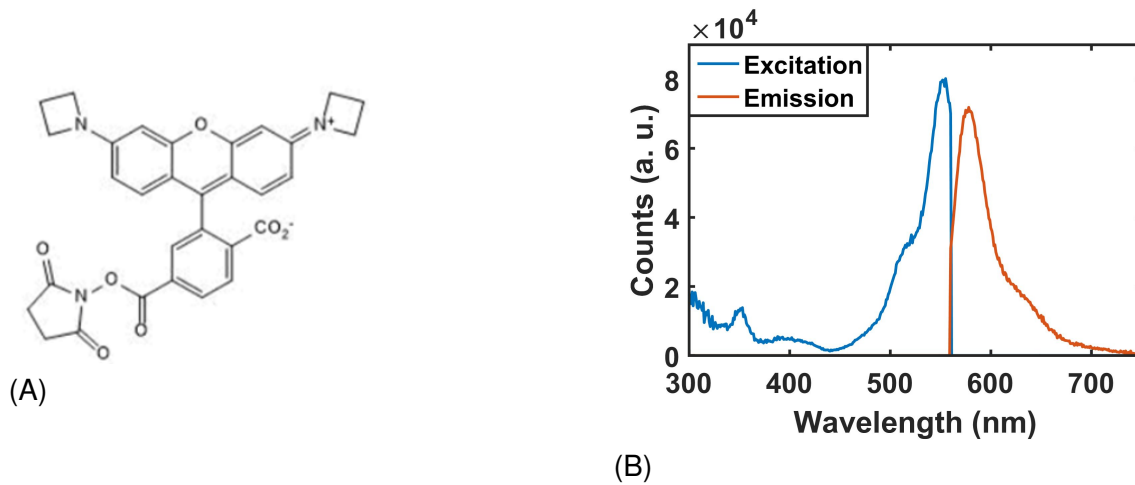


Figure 10: (A) Chemical structural formula and (B) the excitation and emission spectra of the yellow fluorescence dye JF549.^[44]

4.3 Total internal reflection fluorescence microscopy (TIRFM)

The total internal reflection fluorescence microscopy is a useful method for observation and studying of events, which takes place near the coverslip surface such as processes at the PM in live cells.^[45]

The principle behind TIRF is that the excitation beam reaches the interface between the cover slide and the sample, in this case the cells, at a certain angle θ_c to the surface, (see **Figure 11**). The critical angle of incidence is given through the quotient of the refractive index of the liquid medium divided by the index of the substrate:^[48]

$$\theta_c = \arcsin\left(\frac{n_2}{n_1}\right). \quad (1)$$

If the critical angle θ_c is larger than the normal angle, it causes the total reflection of the excitation light with the result of creating an evanescence wave field at the interface, otherwise the beam would pass through the sample. This generated thin electromagnetic field has the same frequency as the incident light and can penetrate the cell up to 100 nm from the coverslip.^{[47] [49]}

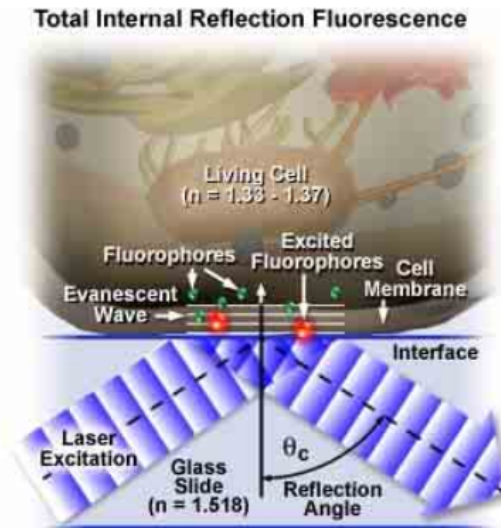


Figure 11: Schematic representation of the total internal reflection fluorescence principle. The laser beam reaches the glass slide at the critical angle θ_c , which leads to the excitation (red) of the fluorophores (green) near the interface by creating an evanescent wave.^[46]

The intensity of the evanescent wave decays exponentially with the perpendicular distance:

$$I = I_0 \cdot \exp\left(-\frac{z}{d}\right), \quad (2)$$

where I is the intensity at one point in space, I_0 the starting intensity, z the distance and d the penetration depth in the cellular medium.^{[36] [47]}

The characteristic exponential decay depth d can be calculated from:

$$d = \frac{\lambda}{4\pi n_2} \cdot \left(\frac{\sin^2 \theta}{\sin^2 \theta_c} - 1 \right)^{-\frac{1}{2}}, \quad (3)$$

where λ is the wavelength of the incident beam in the vacuum, n the diffraction indices, θ the angle and θ_c the critical incident angle.

The decay depth means that only specific fluorescence molecules near the interface are excited, while others inside the cell or the extracellular medium remain dark.^[50] For live cell imaging, we take advantage of this method because only molecules which are close to the PM near the glass slide are visualized. As a consequence, only a small region of the cytoplasm is excited, which avoids interference from deeper regions and leads to better resolution.^[36]

The spatial resolution,

$$\Delta x = 0.61 \cdot \frac{\lambda}{NA}, \quad (4)$$

is dependent on the wavelength λ and the numerical aperture (NA)

$$NA = n \cdot \sin \alpha, \quad (5)$$

where n is the refraction index of the medium and α is the maximal half-angle of the cone of light that can enter or exit the lens. NA characterizes the range of angles over which the system can detect light in form of photons. This means the higher the radius of the objective, the larger the light incidence angle the more photons.

To receive a better resolution it is important to increase the NA by increasing the reflection index. A common method for this is to use an oil immersion objective because the reflection index of oil is with 1.515 is more or less the same as the refraction index of glass. This means that the refraction at the oil glass interface is minimized to avoid reflections. If the indices are different, the light from higher angles will be not collected because of the total internal reflection. As a result only a small amount of the light will reach the lens, the other light is deflected into the glass.^[51]



Figure 12: Illustrations of the beam path in (A) the case that the refractive indexes of glass and immersion medium are the same and in (B) that the reflection index is smaller than the one from glass, for example air(1.0).^[51]

4.4 Fluorescence fluctuation spectroscopy (FFS)

Biological processes in cells usually happen on spatial and temporal scales across different orders of magnitude, with the result that the larger ones are easier to observe than the lower ones.^[52] The information about structure, dynamics and function requires measurement techniques with a spatial and temporal resolution of single-molecules in the range of microseconds to milliseconds.^[56] With light microscopy, it is possible to take images of cells with both requirements, but with a worse signal to noise ratio. The results are far away from the temporal and spatial resolution offered by fluorescence fluctuation spectroscopy (FFS) with a better signal to noise ratio. Confocal laser scanning microscopy

(CLSM) is a widely used technique to measure fast diffusion dynamics of fluorescently labeled molecules in solution or cells. Therefore, the sample is scanned in a raster pattern by a confocal laser beam to measure the fluorescence intensity at different positions. FFS analyzes those recorded fluctuation signals within a cell to resolve the underlying molecular mechanism with different timescales resolution.^[56] The most common methods to analyse fluorescence fluctuations are fluorescence fluctuation correlation spectroscopy techniques, like FCS, ICS or RICS. Those techniques are applicable to a commercially available laser scanning or TIRF microscope based on fluorescently targeted molecules.^[57]

4.4.1 Fluorescence Correlation Spectroscopy (FCS)

Fluorescence Correlation Spectroscopy (FCS) is the measurement of the fluorescence signal fluctuations in a stationary confocal observation volume as a function of time. This method was originally developed by Magde et al.^[53] and later advanced for cells by Berland et al.^[54], 30 years ago to measure fast diffusion and dynamic processes in the microsecond to millisecond time range. The main processes are those where the excited fluorophores of the molecules diffuse in and out the small observation volumes. Out of the recorded fluorescence fluctuation signals an autocorrelation function (ACF) is calculated to obtain information about the underlying molecular process responsible for fluctuations.^[56] However, this method is limited, because it was implemented as a technique to observe a single spot in a static confocal observation volume. As a consequence it is possible to receive a good temporal resolution but with a lack of spatial information.^[56] Hence, other fluorescence correlation spectroscopy methods have been employed to bypass these problems.

4.4.2 Image Correlation Spectroscopy (ICS)

Another FFS method based on image-recording microscope was developed by Petersen et al.^[62] known as Image Correlation Spectroscopy (ICS), which is a powerful mathematical-image processing approach to study the concentration, degree of aggregation as well as the average number of aggregates in a cellular context.

The theory behind ICS is to measure the fluctuation of the fluorescence signal of an excited molecule within a cell between the images collected in a time sequence.^[60] The calculated image spatial autocorrelation function of a static point object is the PSF of the system, often as a 2D Gaussian function.^[58] This means that the PSF should have at least a radius twice than that of the observed signal to obtain a high resolution. The amplitude of the determined 2D correlation peak is inversely proportional to the number of particles

per confocal volume. Deviation from the conditions, for example particle movements, will broaden the correlation peak.^[59] However, the 2D-Gaussian function gives only a plane/beam area, known as pseudo volume, but no information about the z direction. This is due the fact that ICS was developed with the assumption of no movement on the time scale of the frame acquisition.^[61]

4.4.3 Raster Image Correlation Spectroscopy (RICS)

Raster Image Correlation Spectroscopy (RICS) is a combination of FCS and ICS. RICS provides spatially resolved information about molecular dynamics and concentration from images of living cells, accessible to standard confocal microscopes. The major benefits are that RICS provides an intrinsic method to separate the immobile fraction from the mobile one and a powerful technique to distinguish diffusion from binding.^[64]

RICS is based on a laser beam, which scans the sample in a sawtooth pattern. During the scan a space-time matrix out of each pixel is created. With those records it is possible to determine the correlation between the images. For the calculation, one pixel sequence for each pixel delay is normalized by the average intensity squared. This operation has to be repeated for all possible combinations of pixels and line shifts. The procedure for calculating the decay is described as followed: Firstly each frame is individually spatial correlated and then the average of all frames is taken.

Therefore, the movement of the laser by raster the sample is given through the spatial correlation function decay of the scanning part, $S(x,y)$ expressed as:

$$S(x, y) = \exp\left(-\frac{\frac{1}{2}\left[\left(\frac{2x\delta r}{\omega_0}\right)^2 + \left(\frac{2y\delta r}{\omega_0}\right)^2\right]}{1 + \left(\frac{4D(x+ny)\tau}{\omega_0^2}\right)}\right), \quad (6)$$

where x is the horizontal coordinate, y the vertical coordinate, δr the pixel size (typically in the range of 20 to 200 μm), ω_0 the e^{-2} radius of the point spread function of the laser beam, τ the pixel dwell time (normally set in a range of 2 to 100 μs), and n the pixel sequence number.^[55] To know the movement of the scanning beam, it is necessary to distinguish between the laser movement and the Brownian motion of the molecules.

In **Equation 7** the correlation part of the autocorrelation function due to diffusion is given as:

$$G(x, y) = \frac{\gamma}{N} \cdot \left(1 + \frac{4D(x+ny)\tau}{\omega_0^2}\right) \cdot \left(1 + \frac{4D(x+ny)\tau}{\omega_z^2}\right)^{-\frac{1}{2}}, \quad (7)$$

where γ is a factor describing the geometry of the excitation volume and D the diffusion coefficient. [64]

The convolution of the scanning part $S(x, y)$ and the correlation function $G(x, y)$, leads to the overall autocorrelation function:

$$G_s(x, y) = S(x, y) \times G(x, y). \quad (8)$$

As fluorescence-labeled molecules appear generally as small specific spots superimposed on an unspecific background, it is necessary to record many frames to have enough statistics to recover the correlation function from the noise bearing fluctuations. [64]

For a raster scan pattern, the correlation of images appears on different timescale in the range of microseconds in scan direction to seconds between frames (Figure 13). [63] [64]

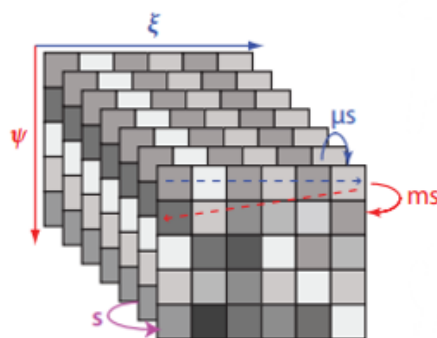


Figure 13: Image recording with a CLSM for RICS. The scanning of the sample occurs in sawtooth pattern by a laser beam. The timescale in scan direction is in the microsecond (blue) range, while between two lines in an image it is in the millisecond (red) range and between frames in seconds (purple). [56]

The points in a RICS image are measured at different positions and at different times subsequently. Hence the timescale between pixels along the horizontal scanning axis is in microseconds, while it takes millisecond to switch from one line to the other and up to seconds to go from one frame to the next. These timescales make it possible to generate spatial-temporal maps of the dynamic inside the cell in the range of microseconds to milliseconds. [65]

This work uses RICS to study the diffusion of fluorescence-labeled components within a cell. The change in particle concentration as a function of time, can be described as:

$$C(r, t) = \left(\frac{1}{(4\pi Dt)^{\frac{3}{2}}} \right) \exp\left(-\frac{r^2}{4Dt} \right). \quad (9)$$

As one can recognize the equation is composed of two terms, a temporal term and a spatial exponential Gaussian term. The concentration C at the position r at time $t=0$ is the probability to find a particle proportional to its diffusion coefficient (D). If the particle is located at this point, its fluorescence intensity is distributed within a distance of r with a Gaussian distribution probability. For any diffusion values, the amplitude decreases as a function of time and the width of the Gaussian increases as a function of time. A 2D-autocorrelation function of the fluorescence decay can be approximated as a function of a characteristic time, which is dependent on the size of the illumination volume as well as the diffusion constant. [55]

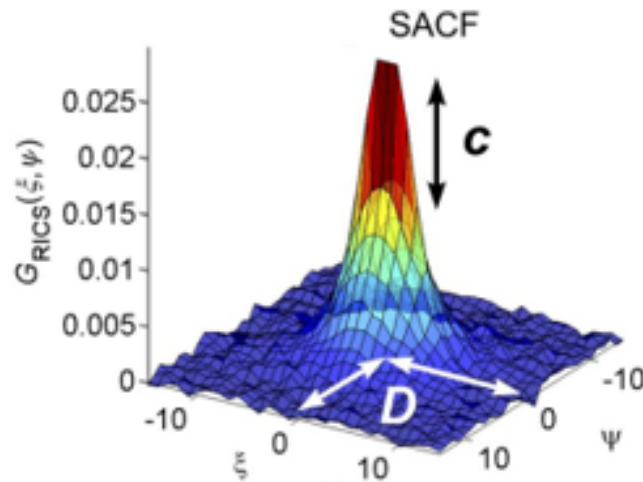


Figure 14: 2D-plot of a calculated spatial autocorrelation function (SACF). The concentration can be determined by the amplitude, while the diffusion over the shape of the decay. [56]

ACLSM sampled different locations which allows the observation of fast moving particles via RICS. This is based on the fact that the recorded intensity at one point is correlated to the intensity of the adjacent point, if the particle is moving. In **Figure 15** 2D-plots are illustrated which show the different shape of fast and slow diffusing particles. The probability to detect slowly diffusing molecules near to the origin is higher than for fast diffusing ones. The latter can be detected further away in scan direction only from their origin because of their fast movement. [55]

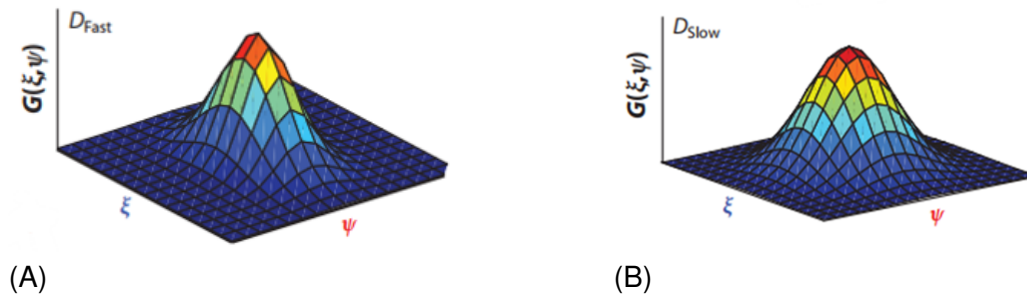


Figure 15: 2D-plots of RICS measurement dependent on the diffusion coefficient. SACF of molecules with (A) a fast diffusion constant and (B) of a slow diffusion constant. [56]

4.4.4 Pulsed Interleaved Excitation (PIE)

With FFS it is also possible to perform multi-color fluorescence experiments by using pulsed interleaved excitation (PIE), to maximize the information retrievable with each photon.^[67] The principle behind PIE is that multiple excitation sources are interleaved. This means that the fluorescence emission generated from one pulse is completed before the next excitation pulse arrived at the detector. This alternating laser excitation (ALEX), where the lasers are turned on separately, was introduced by Kapanidis et. al.^[68]

Hence, the repetition rate is limited on the lifetime of the emitted photons, the advantage of using PIE is that it provides not only a spectral and spatial separation of the fluorophores but also a temporal separation. Additionally spectral cross talk, which can occur when more fluorophores within the cell, can be separated out. This could be for example realized with a two-color detection of the image, where the signals can be split into different detection channels.^[67]

4.5 Wavelet analysis

Fluorescence-labeled particles appear generally as diffraction limited spots in an image. In most cases the signals are superimposed on an unspecific background. For reliable and statistically quantitative results, it is necessary to analysis a large number of frames to minimize the biological influences. One big problem by tracking spots in a movie is that in one part of the image they appear lighter or darker relative to the background. To overcome this problem, filter methods like the wavelet analysis can be used.^[71]

This method features a powerful and fast filter for the elimination of noise, by setting a threshold. Mallat proposed a dyadic and decimated wavelet analysis of discrete signals by splitting the input signal into a low and a high frequency.^[66] The lower signal is than

again divided into a high and low frequency applying a low pass and high pass filter respectively (**Figure 15**)^[66]. This allows to localize the spots at positions, where the response of the filter is above a pre-defined threshold. However, it become less selective in the prescence of objectives with different shapes or size.^{[66] [69]}

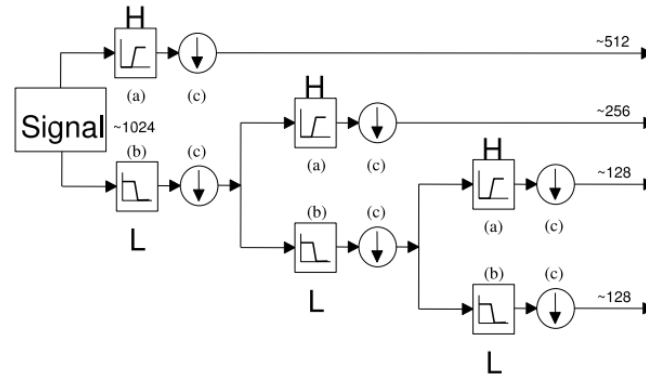


Figure 16: Picture of the wavelet decomposition, filtering the frequency through (a) a high pass and a low pass function followed by (c) downsampling. function^[66]

In this work a method based on a multi resolution analysis tool, which applies a non-decimated wavelet transform, the *à trous* algorithm was used.^[70] The principle behind this algorithm is to implement a separable wavelet, the smoothed approximation. From this smoothed approximation the wavelet plane is computed as:

$$W_1(x, y) = A_0(x, y) - A_1(x, y) \quad (10)$$

where $A_0(x, y)$ is the original image in the first iteration and $A_1(x, y)$ the smoothed approximation. This process is repeated for each image. The out coming *à trous* wavelet representation has the advantage that each wavelet plane has the same number of pixels as the original image. This wavelet transform gives a multiresolution representation of the images. To reduce the influence of noise a threshold can be set to denoise the wavelet coefficient.^[71]

5 Experimental section

5.1 Cell preparation

5.1.1 Materials

The reagents which were used for the cell preparation are listed in **Table 1**.

Table 1: Utilized reagents.

Reagents	Producer
Dulbecco's Modified Eagle Medium	Invitrogen GmbH/Life Technologies (California, USA)
Dulbecco's Phosphate Buffered Saline (- Mg ²⁺ / Ca ²⁺)	Invitrogen GmbH/Life Technologies (California, USA)
Fetal bovine serum (10%)	Invitrogen GmbH/Life Technologies (California, USA)
FluoroBrite DMEM	Invitrogen GmbH/Life Technologies (California, USA)
Optimem	Invitrogen GmbH/Life Technologies (California, USA)
Turbofect	Roche Diagnostics GMBH, (Germany)
Trypan Blue Stain (0.4%)	Invitrogen GmbH/Life Technologies (California, USA)
Trypsin-EDTA (0.05%)	Invitrogen GmbH/Life Technologies (California, USA)
XtremeGene 9 DNA transfection reagent	Roche Diagnostics GMBH, (Germany)
Recovery cell culture freezing medium	Invitrogen GmbH/Life Technologies (California, USA)

All chemicals have been used without any further purification. The cell culture medium, DMEM, which contains 1 g/L D-Glucose and Pyruvate, as supplemented with 10% fetal bovine serum (FBS) and 1x Penicillin/Streptomycin (Pen/Strep). Fluorobrite, the image medium, contains of high D-GLucose and 3.7 g/L Sodium Bicarbonate and was supplemented with 10% FBS, GlutaMAX, HEPES and Pyruvate.

The cell lines, Hela Kyoto, Hela Ad8Eg5.5 and Hela Ad8E, as well as all used plasmids, were provided by the group of Dr. Barbara Müller, University of Heidelberg, Germany.

5.1.2 Thawing

Firstly, the frozen cells were quickly thawed at 37 °C in a water bath before transferred to 1.5 ml warm DMEM medium in a 2 ml reaction tube and then centrifugated at 900 rpm for 5 min. After removing the supernatant, the cell pellet was resuspended in 2 ml warm medium and again centrifuged under the same conditions. Next, the pellet was resuspended

in 5 ml warm medium and transferred to a 25 cm² cell culture flask. For growing the cells were placed in an incubator at 37 °C in a 5% CO₂-atmosphere.

5.1.3 Splitting

Cells were splitted at about 70% to 80% confluency checked by light microscopy. The old medium was aspirated and the cells were washed with 5 ml PBS, without Mg²⁺ and Ca²⁺. The PBS was removed after a short time and 500 µl 0.05% Trypsin was added to coat the bottom of the cell culture flask from which a small amount was aspirated right after. The cells were incubated for 2-5 min before the detachment was checked under the microscope and the reaction was stopped by adding 5 ml DMEM medium and gently mixing. Next, aliquots of the resuspended cells were transferred into a new cell culture flask and the required amount of medium was added. In most cases the cells were splitted in a dilution of 1:10, which means 500 µl cells and 4.5 ml medium, or 1:20, meaning 4.75 ml medium added to 250 µl cells.

5.1.4 Seeding for transfection

Before seeding the cells, the cell concentration was determined. Therefore, 20 µl of the resuspended cells were mixed with 20 µl Trypan Blue Stain, transferred into a cell counting chamber slide (Invitrogen) and measured with a “Countess II automated cell counter” (Invitrogen by thermo scientific).

For a same-day overnight transfection, $2 \cdot 10^4$ cells per well were seeded into one chamber of a Nunc Lab-Tek II Chamber Slide System or in a 96-well plate. The concentration for a next-day transfection was $1 \cdot 10^4$ cells per well. Using Lab Tek II the required volume of medium was added to reach a total amount of 300 µl, in case of 96 well-plate the total amount was set to 200 µl.

5.1.5 Transfection

Cells were transfected 12-24 h before measuring, using a mixture containing the transfection reagent and plasmids in OptiMEM, listed in **Table 2**.

Table 2: Transfection mixture.

Reagent	addition	Concentration stock solution	Dilution	Amount [μ l]
OptiMEM	always			67
XtremeGene 9	always			1.2
pCHIV	partial	1 μ g/ μ l	1:10	3
pCHIV.eGFP	partial	1 μ g/ μ l	1:10	3
peGFP	partial	1 μ g/ μ l	1:10	2
peGFP ₂	partial	500 ng/ μ l	1:5	2
peGFP ₃	partial	500 ng/ μ l	1:5	2
peGFP ₅	partial	500 ng/ μ l	1:5	2
peGFP.GPI	partial	100 ng/ μ l		2
HIV.CLIP	partial	1 μ g/ μ l	1:10	3

The components of the mixture changed according to the planned experiment. For transfecting the cells with pHIV.Gag the labeled plasmids are mixed in a 1:1 ratio with the unlabeled Gag plasmid. In the case of CLIP the labeled pHIV-CLIP and unlabeled Gag plasmid was used.

The steps of preparing the mixture was as followed: Firstly, the OptiMEM was provided in a reaction tube and mixed with XTremeGene9, the transfection reagent, followed by adding the plasmids. After incubating the mixture for 15 min at room temperature (RT), 15 μ l of the mixture was added to each well.

3 to 6 hours post transfection (hpt) the cell medium was aspirated and 200 μ l warm FluoroBrite image medium was added. In comparison to the DMEM medium, the image medium is CO₂-dependend, composed of high D-Glucose, 10% FBS and Pen/Strep but without phenol red and L-glutamine. It is neccassary to change the medium because otherwise phenol red would be excited by the laser and fluoresce, which influences the measurement.

On the next day the samples were measured either with TIRF or RICS without any further preparation, except those which were transfected with pHIV.CLIP. In this case a dye, JF549 or JF646, was added in a concentration of 0.1 or 0.5 μ M. After one hour the cells were washed twice with PBS. Then 200 μ l warm image medium mixed with 100 nM rCD1 was added to the sample.

5.1.6 Freezing

Freezing is a method to prepare cells for long time storage. Therefore, the protocol for cell splitting was used and the detached cells were transferred into 2 ml reaction tubes. After spinning down by centrifugating at 900 rpm for 5 min, the supernatant was removed, and the pellet was resuspended with the appropriate amount of freezing medium, containing 10% DMSO, to reach a cell concentration of $5 \cdot 10^5$ to $1 \cdot 10^6$ cells/ml. Afterwards, the cell suspension was aliquoted into cryo vials and stored at -80 °C.

5.2 Methods

For the measurements with the Ad8E and Ad8Eg5.5 cells the reversible chemical dimerizer system was used. Therefore 100 nM rCD1 was added to the with HIV-1 transfected cells causing the recruitment to the PM of the enzyme phosphatase. This allows a fast and controllable reduction of the PIP₂ level at the PM of virus producing cells.^[22] By converting PIP₂ to PIP through dephosphorylation, some of the already to the PM anchored Gag clusters are dissolved. This leads to the loss of Gag targeting. Restoring the concentration of the PIP₂ level at the inner leaflet of the membrane is possible by adding 100 nM FK506 the competing ligand of rCD1. FK506 displaces the phosphatase and makes it possible for Gag to bind synchronal to the PM.^[2]

5.2.1 TIRFM

All TIRF measurements were performed on a custom build microscope setup. A Nikon Ti ECLIPse body integrated with a PECON incubation chamber, which allows to measure cells at 37 °C and 5% CO₂. An Apo TIRF 100x (NA 1.49) oil immersion objective from Nikon was used. The setup is equipped with 6 diode laser (Cobolt), appropriate filters and 3 EMCCD cameras (Andor) to visualize the signal. As this microscope can be used either for TIRF or WF measurements, it is possible to alter between the different excitations by an electronically triggered shutter.

Most cells were measured for approximately 35 min with 50 ms exposure time and 250 ms interframe time, to reduce photoinduced damage in cells.

For dual-color measuring of Ad8E cells transfected with pCHIV.eGFP, the yellow 561 nm laser (0.5-2 mW) was used in combination with a 580 to 620 nm filter to visualize the with mRFP labeled enzyme phosphatase. By using this filter only the emitted photons of the excited mRFP arrived at the detector. The blue 488 nm laser (2 mW) with a filter in the range of 500 to 550 nm was used to excite eGFP producing cells at the PM (**Figure 17**).

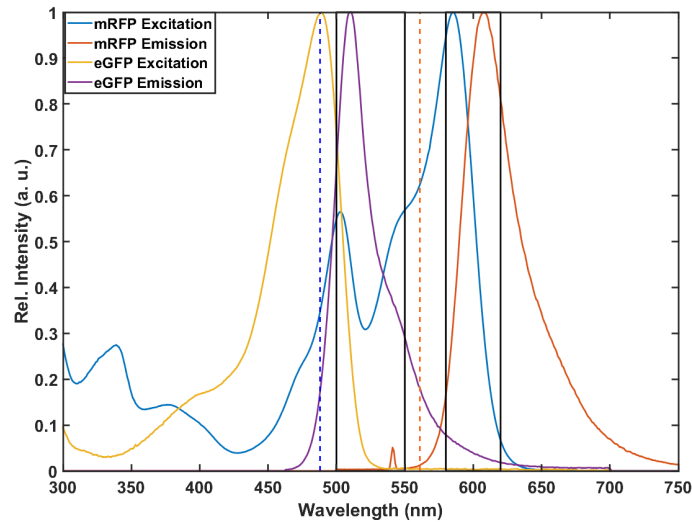


Figure 17: The excitation (yellow) and emission (purple) of eGFP and mRFP (blue /red). In addition the excitation wavelength of eGFP (blue dashed line) and mRFP (orange dashed line). It is nicely represented that the respective emission is in the range of the used filter (black box).

To synchronize the assembly, 100 nM rCD1 was added 3-6 hpt and 100 nM FK506 was pipetted to the samples just before measuring. The images were recorded using alternating-laser excitation (ALEX). This means that lasers were turned on separately. Normally the exposure time was set to 50 ms and the interframe time to 250 ms. The measurement time was set to about 45 min and 4.000 frames were recorded.

A CLIP system in combination with the JF646 dye was used to image the Ad8Eg5.5 cells, where the phosphatase was labeled with eGFP. The phosphatase was excited by a blue 488 nm laser with approximately 2 mW laser power. JF646 was excited with a 642 nm red laser and a filter in the between 650 nm and 800 nm was used. The protocol of the measurement was the same than for the Ad8E cells. Firstly, 100 nM rCD1 was added and shortly before the measurement started 100 nM FK506 was supplemented.

5.2.2 RICS

The used microscope for the RICS measurements was a custom build CLSM, with a Nikon 200 body and a heatable stage. For the measurements a Apo TIRf 100x (NA 1.49) oil immersion objective from Nikon was used.

The scan speed of the laser should be set dependent on a priori knowledge of the diffusion of the molecules. 4 $\mu\text{s}/\text{pixel}$ scan speed is normally used for fast molecules, with a diffusion coefficient higher 100 $\mu\text{m}^2/\text{s}$, compared to 8-32 $\mu\text{s}/\text{pixel}$ for slower molecules

and up to 100 $\mu\text{s}/\text{pixel}$ for very slow molecules with a diffusion coefficient in the range of 1 to 10 $\mu\text{m}^2/\text{s}$. A common mistake is to set the scanning speed too low, which causes a not meaningful result.

Before the measurements started, the microscope had to be calibrated. Therefore, a well of a LabTek slide was coated with 20 μl BSA (2mg/ml) and after 30 min washed with ddH₂O. For the calibration, 5 μl 5 nM Atto 488, 15 μl 5 nM Atto 565 and 1 μl 5 nM Atto 655 were added together and measured. Afterwards, the measurements of the transfected Ad8E cell were performed. As we were interested in the process after the addition of rCD1, we added 100nM rCD1 just before and measured the cytosol of the cell. For the visualization of the phosphatase, the yellow laser (561 nm Toptica) was used. The blue (492 nm Picoquant) laser was used to image either the with eGFP-labeled HIV particles or the JF549 and in case of JF646 the (630 nm Picoquant) was used. The settings for the measurements were as followed: 150 frames (300 x 300 pixels) were measured six times including a 2.5 min break between the cycles to a total of 30 min, with a laser power of 2 μW and a frame time of 1000 ms as well as a pixel size of 40 nm.

5.3 Analysis

All recorded frames from the TIRF as well as from the RICS measurements were analyzed via MATLAB (MathWorks) or MATLAB based programs.

5.3.1 Analysis of the TIRF data

Firstly, the recorded image stacks were examined with ImageJ and those cells where particles attached to the PM during the measurements were analyzed. Therefore, the frames of one measured cell were uploaded in a MATLAB program and tracked with a custom wavelet transform filtering method, the *à trous* algorithm.^[70] The wavelets 2 and 3 were taken for the tracking of a 96 nm pixelsize image with 100 x magnification.

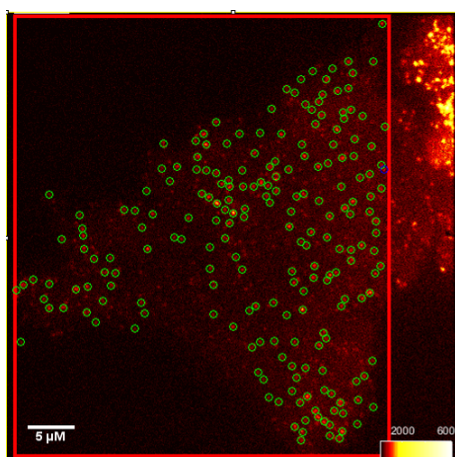


Figure 18: The results of the tracking program. The image series is loaded and with setting the red box, the region is selected where the tracking should be done. The green dots represent spots which are tracked over longer frames and in blue those over less than four frames.

After loading the image movie into the program, the region where the tracking should be performed was selected by setting the red box. The green spots in **Figure 18** represents the particles which were tracked over a longer frame series, while the blue ones are lost after less than four frames.

Next, the intensity traces of the tracked particles were created using a circular 3X3 small mask with a background correction. By setting a threshold only the traces of particles, which were tracked over 100 frames or more were plotted. After this step the average of the normalized intensity of all tracked particles were plotted against the time.

The traces, with an continuous intensity increase or a jump in the intensity progression were further analyzed, by finding the particle in the movie. The traces of each particle,

which was not present from the beginning and was clearly identified as one particle, was selected. The intensity of all selected particles were plotted against the time.

Assembly kinetics were determined from these intensity plots by using the MATLAB curve fitting toolbox. The curve was fitted with the following logistic growth equation:

$$y = f(x) = a \cdot (1 - \exp(-b \cdot x)) + c, \quad (11)$$

where a is the maximal value and c the offset. The assembly rate of the clusters at the PM was given directly through the coefficient b . The different frame times were already considered by plotting the averaged intensity against the time in seconds.

5.3.2 Analysis of the RICS data

The recorded frames were uploaded into the MATLAB based program ‘PIE-Analyses with MATLAB’ (PAM). This program reconstructs the pixels by reassigning the photons into bins based on the pixel dwell time. Additionally, the program plotted the photon count histogram against the TAC range of the measured signal of each channel. Ranges were set based on delay of laser for PIE (**Figure 19**). The signal of the yellow channel consist of two peaks. The smaller peak at a lower tac range results from the cross talk with the blue channel and the second higher one is the actual signal. The results were saved as Tiff files.

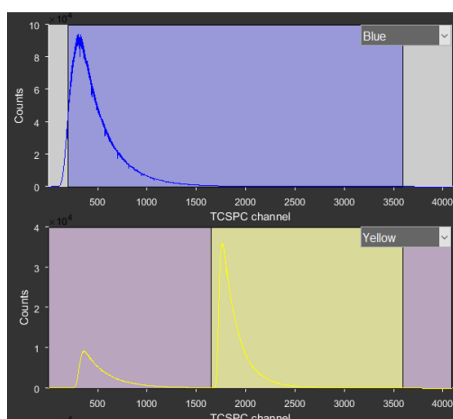


Figure 19: Decays of the signal of the blue and the yellow channel in PAM. The ranges of the yellow channel were set based on the signal delay, which means by separating the signal after yellow excitation of the cross talk after blue excitation.

Those Tiff files were then loaded into ‘micro time image analysis’ (MIA) to perform correlation calculations. The correlation function is calculated on each image individually. By setting a minimum and maximum threshold of photons, corrections can be made in

movies by omitting the nucleus and bigger aggregates as well as extracellular space out of the image series before the autocorrelation function was calculated by the program.

For the fitting of these autocorrelation functions, it was necessary to determine the parameters of the observation volume before. Therefore the calibration files were loaded into FCSFIT and fitted by fixing the PSF ω_r/ω_z of each channel. As the calibrations were performed under room temperature the diffusion constant of Atto 488 was set to $393 \mu\text{m}^2/\text{s}$ and for Atto 565 to $373 \mu\text{m}^2/\text{s}$. As a result the size of the observation volume was obtained by the axial ω_z and lateral ω_r focus radii.

Next the autocorrelation function of the each measurement time point of a cell measurement were fitted with MIAFit. As the parameters of the observation volumes were fixed, it was possible to calculate the mobile and immobile fraction by using a two-component fit. The immobile fraction was fitted as 2D Gaussian function where the parameter ω_{imm} indicates the half-width of the function at $1/e^2$ of the maximal intensity of the immobilized species. The number of mobile objects is defined as the average number of molecules in the PSF, which have a diffusion constant higher than $0.3 \mu\text{m}^2/\text{s}$, limited by moving imaging correction.^[75] Beside the mobile and immobile fraction, also the brightness as well as the diffusion coefficient of each image series was obtained from the fit.

6 Results and discussion

6.1 Aim

In this thesis, HeLa Kyoto, HeLa Ad8E and HeLa Ad8Eg5.5 cells were prepared and transfected with HIV-particles to study the early assembly of Gag to the PM, the first step of the virion morphogenesis. Therefore, the cells were measured either with TIRF or RICS to research the process and kinetics behind this molecular mechanism.

6.2 Results of the TIRF measurements

6.2.1 Transfection optimization

For the first measurements of transfected cells at the TIRF set-up, Turbofect was used as transfection reagent. The transfection efficiency was not as high as expected, shown in the scan of the dual-color experiment of one well of pCHIV.eGFP transfected Ad8E cells (**Figure 20**). In the scan all cells with an anchor-mRFP are in purple and the eGFP signal is shown in green.

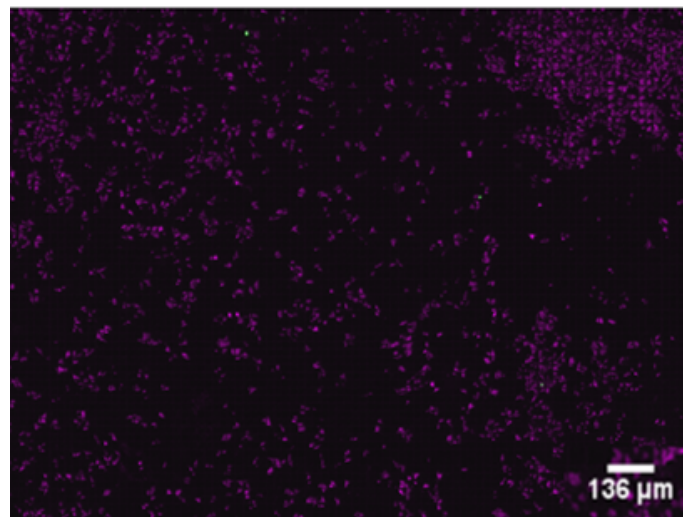


Figure 20: Scan of Ad8E cells in purple and the transfected cells are shown in green.

To increase the transfection rate, the reagent was changed to XTremeGene 9, with the result that more cells were transfected, as seen in the following scan (**Figure 21**). Cells, consists of the anchor-mRFP are in purple and the eGFP signal of the transfected ones are in green. For all following TIRF measurements, as well as for the RICS measurements, XTremeGene9 was used as transfection reagent.

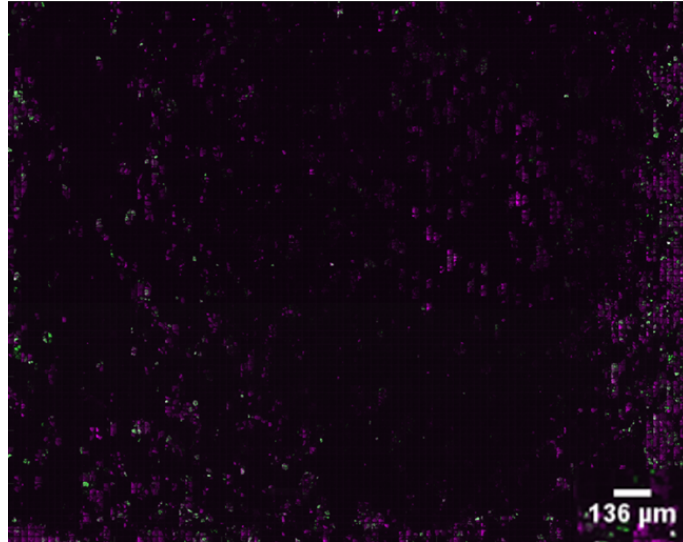


Figure 21: Scan of the Ad8E cells (purple) transfected with pCHIV.eGFP (green).

6.2.2 Statistic of measured cells

Hela Kyoto and Ad8E cells transfected with pCHIV.eGFP were measured at 37 °C and 5% CO₂. The exposure time for all measurements was set to 50 ms and the interframe time to 250 ms. In the case of Ad8E cells ALEX was used, which means that the interframe time increases to 500 ms.

In order to make a statement about the assembly process, several cells were measured to obtain a meaningful statistic. The measured cells were then divided into three categories: cells with new particles, cells without new particles and cells, which die during the measurement.

The classification into the respective categories has been made on the basis of the present of new particles and the structural change of the cell during the measurement.

The time course of a promising measurement, where many assembly sites appear to the PM during the measurement time is shown below (**Figure 22**). In this case the assembly occurs synchronized after addition of the competing ligand FK506.

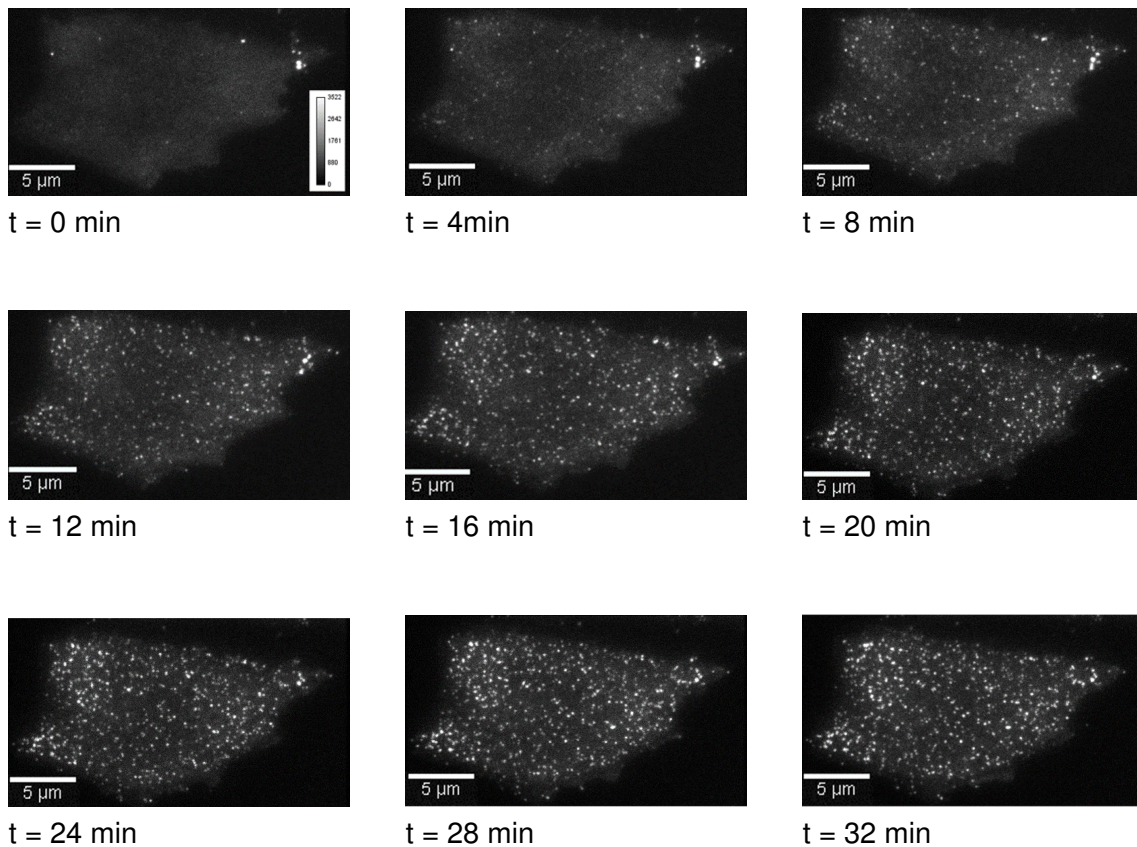


Figure 22: Time course of a transfected Ad8E cell, showing the increase of HIV-particles (white) at the PM during the measurement.

The categorization of the cells without new particles was done by manually screening the videos, from the first frame to the last. If no significant number (> 5) of particles appeared at the PM during this time, the cell was counted to cells without new particles (**Figure 23**).

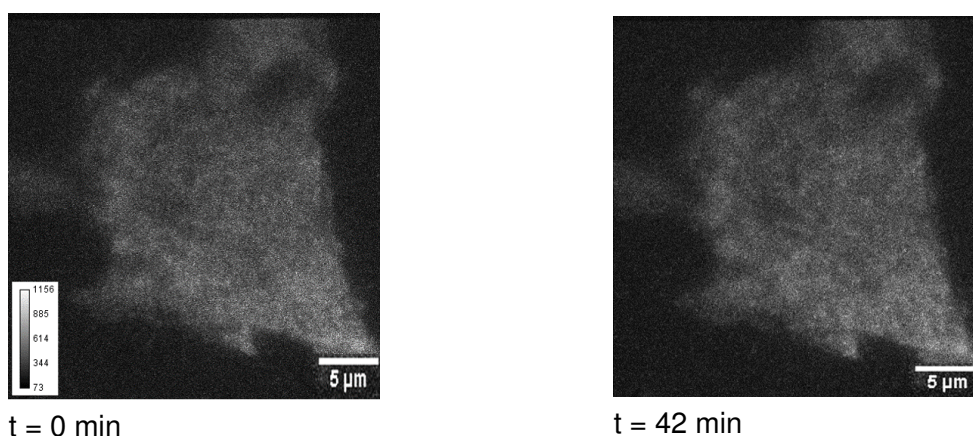


Figure 23: The first and the last frame of a measured transfected Hela Kyoto cell were no new particle arrived at the PM.

Ellipse structural changes of the cells, including the contraction of the PM, causing the

cell to shrink. This indicates that the cell might have undergone apoptosis during the measurement period (**Figure 24**).

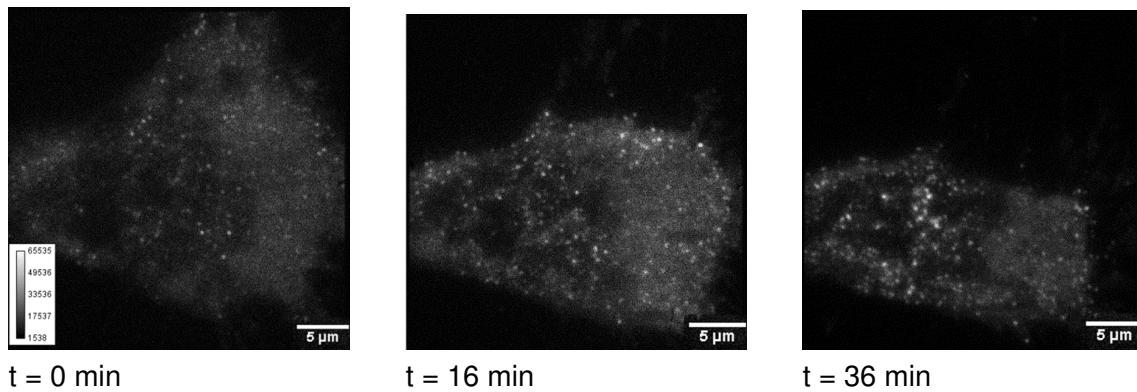


Figure 24: Images of a shrinking HeLa Kyoto cell.

Figure 24 shows nicely how the structure of a cell is changing during the observation time. As one can recognize the number of particles at the PM increases. In this case it is hard to distinguish if the particles just appeared at the PM or comes from the contraction of the cell. Hence, only cells where new particles arrived and which do not changed morphology significantly during the measurements were used for the analyzes.

In **Table 3** the results of all pCHIV.eGFP transfected HeLa Kyoto and Ad8E measured cells are given. **Table 4** shows in comparison to that only the statistic of the with XTremeGene 9 transfected cells.

Table 3: Statistic of measured HeLa Kyoto and Ad8E cells.

cell line	HeLa Kyoto	Ad8E
measured cells	34	50
cells with new particles	19	30
cells without new particles	6	15
cells dying during the measurement	9	5

Table 4: Statistic of the measured cells, were only XTremeGene 9 was used as transfection reagent.

cell line	HeLa Kyoto	Ad8E
measured cells	23	47
cells with new particles	15	29
cells without new particles	3	13
cells dying during the measurement	5	5

6.2.3 Intensity traces

As we were interested in the intensity change of a particle over the time, the intensity traces of the tracked particles were extracted out of the images. As a criteria, only traces where the particle was tracked for at least 100 frames and additionally shows an increase in intensity, were selected. The intensity of the selected particles shows either a continuous rise or a 'jump', examples given in **Figure 25**.

The selected traces of both cell lines were divided into those two categories (**Table 5**).

Table 5: Statistics of selected particles for different cell lines.

cell line	Hela Kyoto	Ad8E
tracked particles	1933	4877
selected particles	63	218
continuous traces	56	185
jumps in the traces	7	35

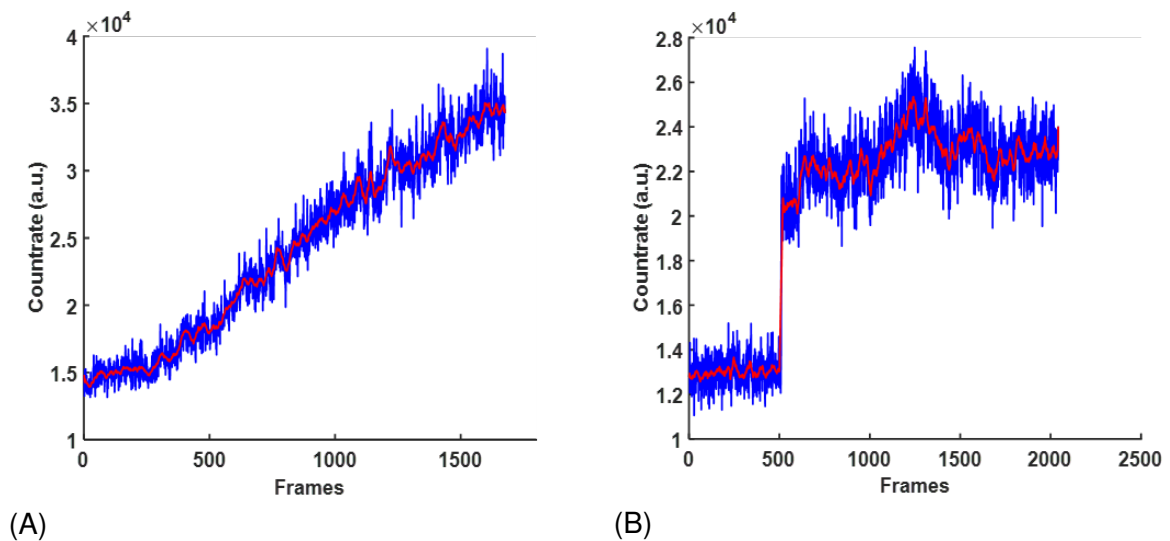


Figure 25: Two different kinds of traces, the continuous rise of the countrate (A) and a "jump" in the trace (B).

In both traces (**Figure 25**) can be seen, that there is a low constant countrate at the beginning and with the time it comes to an increase. The rise of the countrate appears when the Gag.eGFP is the first time tracked by the program.

Conclusions can be drawn from the curve progression with regard to the structure of the attached Gag polyprotein. If the trace shows a continuous process, it is a sign that the Gag assembles as monomer to the PM. While for particles with a step in the trace, it is more likely that the Gag forms cluster in the cytosol that attach to the PM.

From the number of continuous traces in comparison to those with steps (**Table 5**), one might assume that the majority of the assembly sites at the PM are built up from monomeric Gag, either from the cytosol or already attached to the PM.

To directly investigate this assumption, the brightness of monomeric eGFP₁, pentameric eGFP₅ and nonmeric eGFP.GPI, (a membrane anchor), were measured via TIRF.

For the calculation of the counts per molecule the recorded images were fitted via image correlation to generate an autocorrelation function. The molecular brightness in kilo-counts/s/molecule was given through the amplitude of the autocorrelation function. To obtain the counts/molecules independent of the time, the molecular brightness was multiplied by the framerate (**Table 6**).

Table 6: Determined average intensity of eGFP₁, eGFP₅ and eGFP.GPI.

protein	Exposure time (ms)	Brightness (kc/s/molecule)	counts/molecule
eGFP ₁	5	15.58	0.078
eGFP ₁	10	27.46	0.27
eGFP ₁	50	22.97	1.15
eGFP.GPI	5	40.02	0.20
eGFP.GPI	10	84.74	0.85
eGFP.GPI	50	88.79	4.44
eGFP ₅	5	92.96	0.46
eGFP ₅	10	130.79	1.31
eGFP ₅	50	124.29	6.21

Ten cells for each condition were carried out to obtain good statistics. The results revealed that the calculated counts/molecules of the eGFP₅ is five times higher than for eGFP₁. The anchor eGFP.GPI is in the middle of those two, with a factor of three higher than the eGFP₁. This was expected due to the number of fluorophores of the individual proteins

The average counts/molecules of eGFP.GPI, as the size is similar to Gag, was than used to convert the countrate of the intensity traces (**Figure 25**) into GFP. equivalent units (G.E.U.). Therefore, the countrate of each frame of an intensity trace was multiplied by the pixelsize of the used particle mask for tracking, in this case 45, followed by the conversion factor 46.71. The results were then multiplied by the average counts/molecules to determine the G.E.U. The calculated G.E.U. were plotted against time. (**Figure 26**).

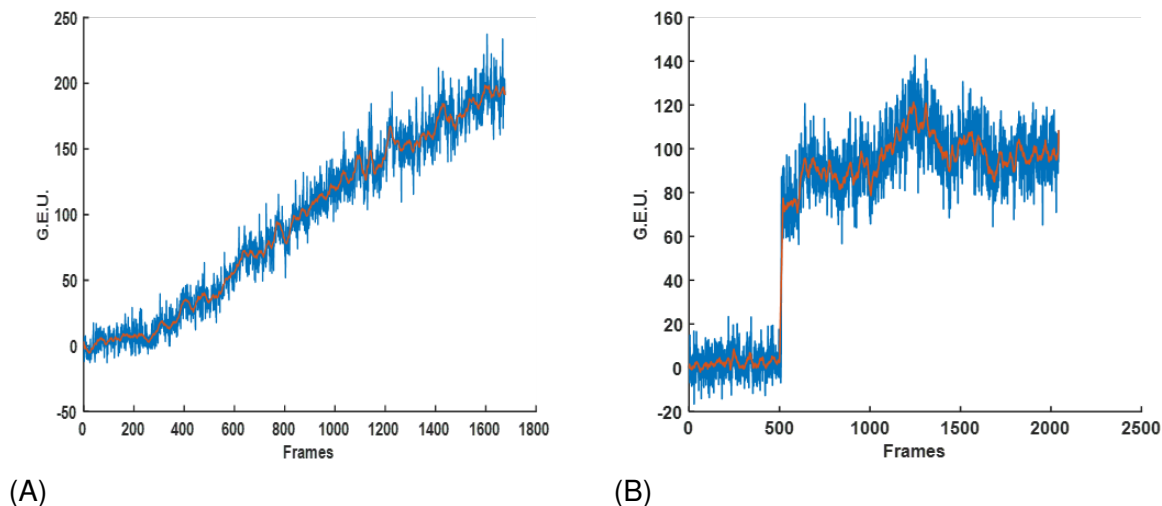


Figure 26: The normalized plots of (A) a continuous trace and (B) a "jump" in the trace. The measurements were started, when 100 nM FK506 was added.

On the basis of the diagrams it is well represented, that the number of Gag molecules at the PM increases over the time. As the results were normalized, the trace starts with zero Gag molecules at the PM. In the case of the continuous trace, one can see that after a time the number of molecules increases continuous and during the first 1800 frames approximately 200 Gag molecules attached to the PM. Due to the gradient, one would assume that Gag binds as monomer to the PM. By reason of the fact that the fluctuations are higher than monomeric brightness, steps in the curve progression are not seen. If steps were seen in the curve progression, it would be easier to make an assumption.

In the case of the particles with a "jump", it is easier to interpret the results. As one can recognize in **Figure 26 B**, the Gag intensity at the PM rises at around 200 frames, which is nicely represented by the high increase in G.E.U. The number of molecules at the beginning of the trace is zero and after the jump the number rises up to 80 G.E.U. This means, that a larger Gag cluster appeared at the PM, which means that the oligomerization must have taken place earlier in the cytoplasm.

6.2.4 Assembly kinetics

For the determination of the assembly kinetics of Gag to the PM, the average intensity of all assembly sites was plotted against time. During analysis, two plots for each promising cell were generated. On the one hand, an intensity plot of all tracked particles and on the other hand only of the selected particles, continuous or jump, were plotted. (**Figure 27**)

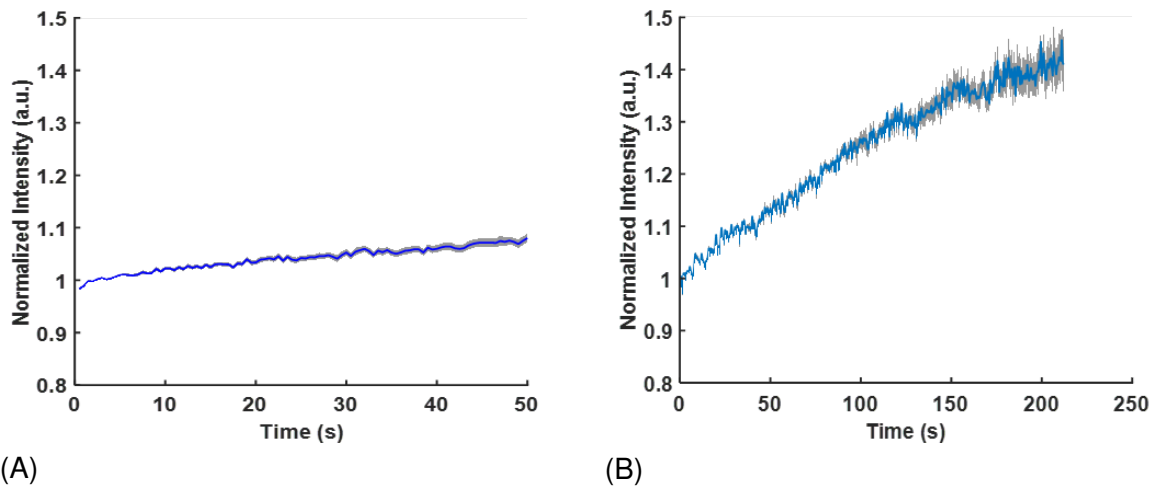


Figure 27: Plot of the normalized intensity against the time for all tracked particles (A), and for only the selected particles (B). The start point of each intensity trace is the first time when the particle was tracked.

The diagrams in **Figure 27** represent the results from a with pCHIV.eGFP transfected Ad8E cell, where for the first plot 258 particles were taken and the second one was generated out of 25 selected traces.

The second plot was used to determine the assembly rate by fitting the curve with a MATLAB based curve fitting program. The calculated results for both fitted plots of the analyzed Hela Kyoto cells, as well as for the Ad8E cells, are given in **Figure 28**.

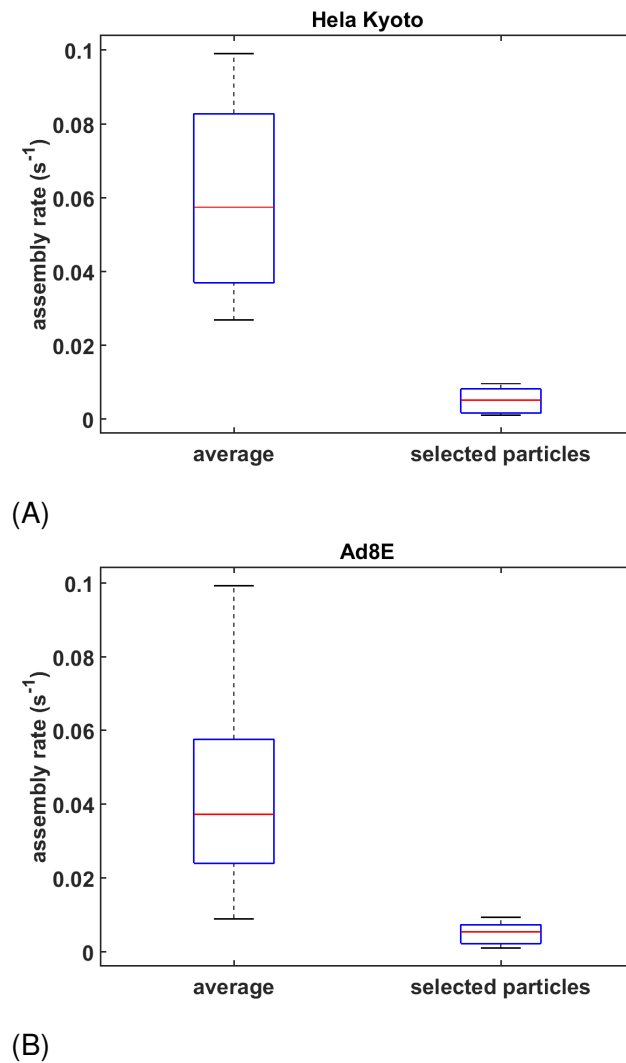


Figure 28: Diagrams of the determined average assembly rate and the assembly rate of the selected particles of (A) Helia Kyoto cells, and in (B) of Ad8E cells.

In the figures above it is well represented that the assembly rate of the Gag binding to the PM is in both cell lines slower for the average of all tracked particles compared to the selected ones. This was no surprise as it was already evident in the corresponding diagrams. It can be seen from the plots (**Figure 27**) that the slope of intensity in the case of selected particles increases more rapidly over time, which also confirms the determined kinetics. The average assembly rate of the selected particles is with $5.2 \cdot 10^{-3} \text{s}^{-1}$, for Helia Kyoto cells, and $5.3 \cdot 10^{-3} \text{s}^{-1}$, for the Ad8E cells very similar. The received values are in good agreement with the published literature. In literature the kinetic of the Gag attachment is in the range of approximately 4.5 to $5.3 \cdot 10^{-3} \text{s}^{-1}$. [2][30]

From this results, we conclude that the anchoring of the HIV-particles to the PM occurs very fast, regardless of whether the assembly happens synchronous or stochastic.

6.2.5 Release of Gag clusters by addition of rCD1

Beside the binding of the Gag to the membrane, we were also interested in the "release" process, which occurs after the addition of rCD1. TIRF measurements of pCHIV.eGFP transfected Ad8E cells were carried out by adding 100 nM rCD1 shortly before. The first and the last frame of one measurement is shown in **Figure 29**.

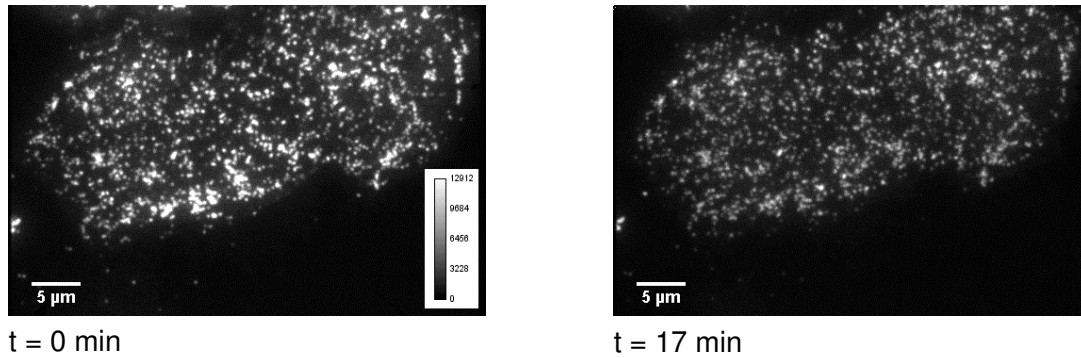


Figure 29: Images of an Ad8E cell after the addition of 100 nM rCD1. The measurements were performed at 37 °C and 5% CO₂ recorded with an exposure time of 50 ms and an interframe time of 500 ms.

By means of the recorded images above, one can see that the number of particles binding to the PM decreases with the time caused by PIP₂ depletion. This observation was expected and is also represented in the following plot (**Figure 30**).

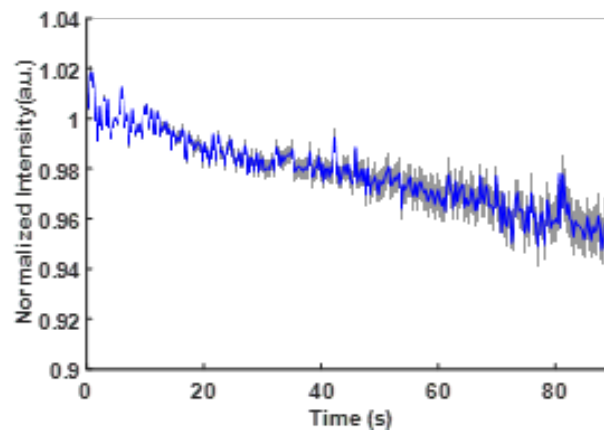


Figure 30: Diagram of the normalized intensity of all tracked particles against the time for an Ad8E cell after adding 100 nM rCD1.

Since it is tedious to see the decrease with free eyes, the particles were tracked with MATLAB. In this case the tracking program found in total 157 traces, in which the particles were present over at least 100 frames. At the beginning the number of particles was 68 and in the end 141. 56 particles were present from the first to the last frame. The higher

amount at the end could be explained by the fact that the clusters, which released from the PM, break up into individual particles. After 90 s the total number of Gag clusters anchored into the inner leaflet of the membrane has decreased by approximately 4%, (seen in **Figure 30**). To be able to make precise statements about the process after the addition of rCD1 the measurements were repeated with RICS to observe the process inside the cell, more precisely in the cytoplasm.

6.3 Results of the RICS measurements

RICS experiments were performed to observe the dynamics of the dissociation process of Gag clusters from the PM after the addition of rCD1.

6.3.1 Diffusion coefficient

To determine the diffusion coefficient of Gag.eGFP alone the experiments were performed with eGFP, eGFP dimer and eGFP tandem trimer (**Table 7**).

Table 7: Diffusion coefficient of eGFP, eGFP dimer and eGFP tandem trimer at 37 °C.

cell	$D_{\text{eGFP}} (\mu\text{m}^2/\text{s})$	$D_{\text{eGFP}_2} (\mu\text{m}^2/\text{s})$	$D_{\text{eGFP}_3} (\mu\text{m}^2/\text{s})$
1	29.41	23.27	12.32
2	31.05	20.04	12.84
3	22.84	18.48	17.75
4	28.48	22.26	17.87
average D	27.93 ± 2.55	21.01 ± 1.75	15.19 ± 2.62

The obtained diffusion coefficient of eGFP with $27.93 \pm 2.55 \mu\text{m}^2/\text{s}$ is higher than the Gag mobility study by Larson et al., who received a diffusion of $D = 23 \pm 5 \mu\text{m}^2/\text{s}$.^[74] The experiments in literature were performed at 26 °C, while we measured under 37 °C. So, it is no surprise that the obtained diffusion coefficient is higher, because with increasing temperature the molecules diffuses faster. Also the eGFP₂ diffusion value of $21.01 \pm 1.75 \mu\text{m}^2/\text{s}$ in the cytoplasm of live cells is higher compared to the published literature, $D = 21 \pm 5 \mu\text{m}^2/\text{s}$.^{[55][72]}

eGFP₃ displays a mobility of $15.19 \pm 2.62 \mu\text{m}^2/\text{s}$, which is significant higher compared to published results, $D = 9.5 \pm 1.5 \mu\text{m}^2/\text{s}$.^[5] This aberration could be also explained by the fact of the different measurement temperatures.^[73]

The obtained results revealed that the diffusion coefficient decreases with higher mass.

The mobility of eGFP with a mass of 26.9 kDa is significant higher than for eGFP₃, which has a mass of 90 kDa. On the basis of those results it is well represented, that the smaller the protein the faster its mobility.

The mobility of monomeric pCHIV.eGFP should be similar to eGFP₃, because the construct has more or less the same size. To directly investigate this assumption and to get a better statistic six cycles of each with pCHIV.eGFP transfected cell were measured and the diffusion coefficient was calculated by image correlation. (**Figure 31**, **Figure 32**).

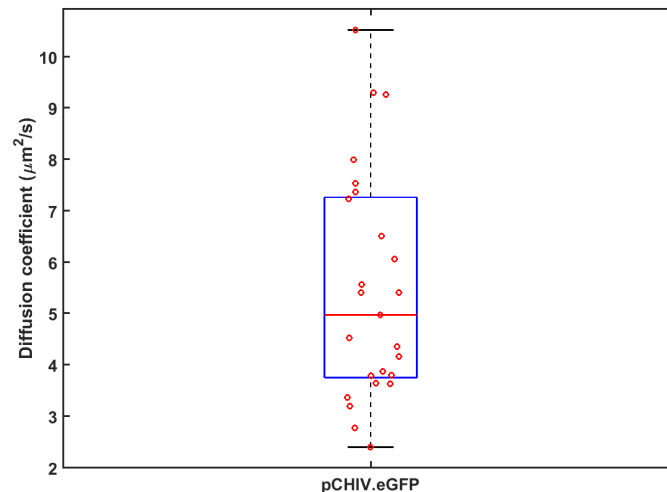


Figure 31: The diffusion coefficient of all measured Ad8E and Ad8Eg5.5 cells transfected with pCHIV.eGFP plotted as a whisker-plot with standard variation. The values of each cells are given in red circles.

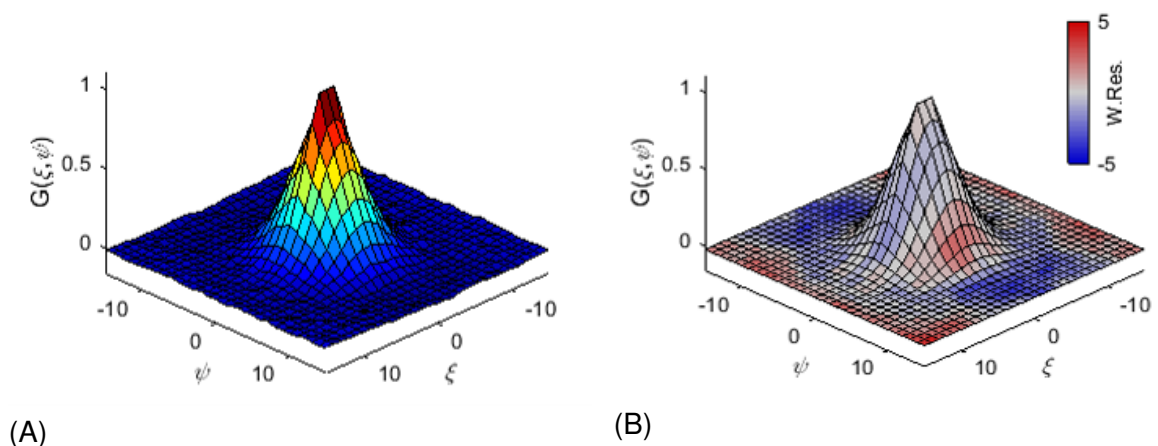


Figure 32: The spatial autocorrelation of pCHIV.eGFP, where ξ and ψ are the spatial lag time in the x and y direction. In (A) the 2D plot of the spatial correlation function is shown and in (B) the fitted correlation with a color-coded goodness-of fit. Gray illustrates a good fit, while red and blue regions indicates higher residuals.

The analysis revealed that Gag diffuses, with an average diffusion coefficient of $5.66 \pm 2.13 \mu\text{m}^2/\text{s}$, slower through the cytoplasm than eGFP₃. From literature we know that Gag binds to the RNA and many other components, which could potentially explain the differences in mobility, due to the fact that Gag clusters could be larger in size compared to eGFP₃.

In comparison with published values in the range of 6-7 $\mu\text{m}^2/\text{s}$ the received results are a little bit lower.^[5] This was unexpected, due to the fact that the literature experiments were performed at lower temperature. A presumption for this result could be that the binding affinity of Gag increases with higher temperature. As a consequence the size of Gag is larger, which may cause a raise of transient interaction within the cytoplasm. The more Gag interacts with other molecules the slower its mobility.

Based on the previous results, the measurements were also performed with pCHIV.CLIP and two different dyes, JF549-CLIP and JF646-CLIP (**Table 8**).

Table 8: Diffusion coefficient of the pCHIV.CLIP induced cells with different dyes.

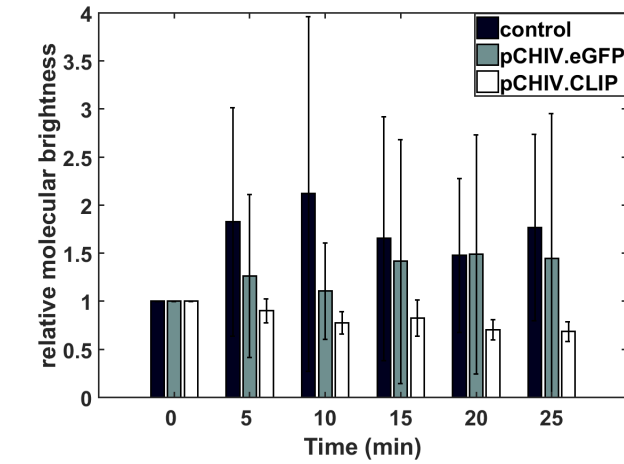
Dye	Cell	average D $8\mu\text{m}^2/\text{s}$
JF 549	1	7.63 ± 1.27
JF 549	2	5.63 ± 0.85
JF 549	3	6.38 ± 0.674
JF 646	1	5.74 ± 0.57

In **Table 8** one can see that the diffusion coefficient of cells transfected with pCHIV.CLIP in combination with a dye do not differ greatly from the mobility of the pCHIV.eGFP cells. As the two constructs have a similar molecule mass this result was expected and shows that the experiments could be also performed with pCHIV.CLIP. By measuring with pCHIV.CLIP the signal to noise ratio was better compared to pCHIV.eGFP, as no full labeling is required. This means that the concentration of the dyes are lower during the measurements and controllable by the amount of addition. As a result the determined correlation curves are better, which causes more accurate data. In order to be able to make more precise statements, it would be necessary to measure more cells to increase the statistic.

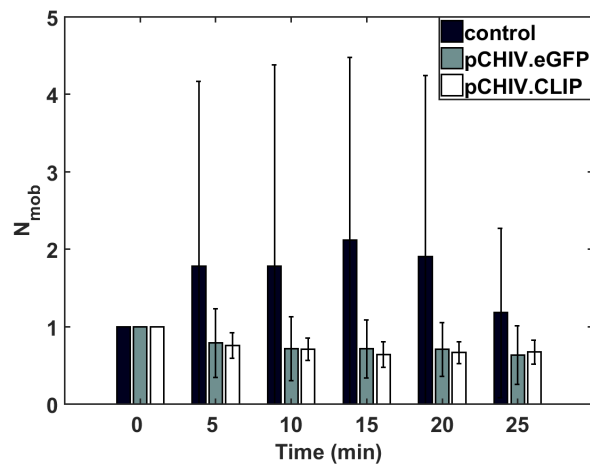
6.3.2 Cytosolic Gag concentration after cluster detachment via rCD1

To study the process behind the depletion of Gag by adding rCD1, the concentration of Gag in the cytoplasm of transected cells were measured. Therefore, Ad8E and Ad8Eg5.5 cells either transfected with pCHIV.eGFP or pCHIV.CLIP were measured. All measurements were started immediately after the addition of 100nMrCD1, except for the control measurements, where no rCD1 was added. The calculated data were normalized to put the different cases into relation. As a reference the average of the first 2.5 min of each measurement was taken, because we know, that it takes a little bit until something happens. The determined normalized molecular brightness, mobile fraction and immobile fraction were plotted against the time (**Figure 33**).

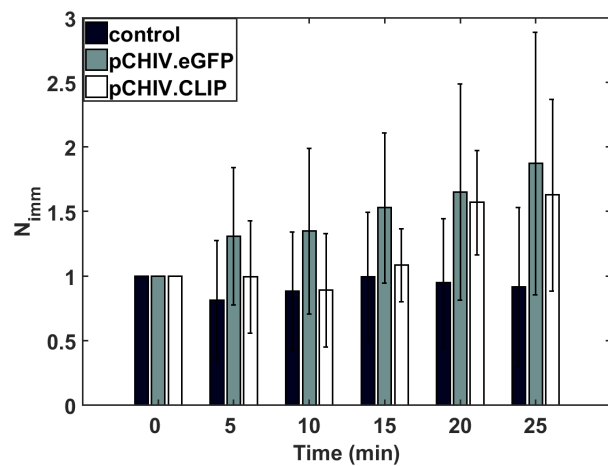
The immobile fraction is defined as species which have a mobility slower or equal to $0.3 \pm 0.1 \mu\text{m}^2/\text{s}$.^[75] It follows, that components with a diffusion coefficient higher than $0.3 \mu\text{m}^2/\text{s}$ are among to the mobile fraction.



(A)



(B)



(C)

Figure 33: The normalized average results of all measured cells were plotted together as barplot with errorbars. In (A) the time is plotted against the relative molecular brightness, in (B) against the number of the mobile fraction and in (C) against the number of the immobile components. All measurements were started at point 0. In the cases of pCHIV.eGFP and pCHIV.CLIP with the addition of rCD1.

By means of the previous plots, no definite trend can be seen in the case of relative molecular brightness (**Figure 33, A**). The molecular brightness of the pCHIV.eGFP and pCHIV.CLIP measurements are more or less constant over time. In comparison to this, the brightness of the control measurements increases during the first ten minutes followed by an decrease. A possible reason for this result could be the protein synthesis of Gag, which takes place in the cytosol. To investigate this assumption the measurements have to be repeated with protein inhibitors to avoid the protein synthesis during the measurement.

In contrast to the molecular brightness, the mobile fraction, as well as the immobile fraction, shows a trend. It stands out, that the amount of mobile species in the cytoplasm declines by adding rCD1 while the number of slow moving particles increases. In contrast to that, the results of the control measurements show a contrary trend, an increase in the number of mobile fraction and a more or less constant immobile fraction over the time.

This results suggest that Gag detaches as cluster from the PM, or as monomers, which immediately binds again to other Gag to form clusters. The cluster size influences the mobility, the larger the Gag the slower it diffuses. Maybe the mobility is too slow, with the result that the Gag clusters, which detached from the PM, are count to the immobile fraction rather than to the mobile one. This could be an explanation for the contrary trend of pCHIV.eGFP compared to the control measurements.

7 Conclusion and outlook

HIV is of high interest in scientific research because many people are affected by this virus. To help them, it is important to understand the molecular mechanism behind the virus development, especially the morphogenesis. With the goal to use this knowledge for producing vaccines against HIV. Nowadays it is known that the formation of an immature to a mature and infectious virus occurs in three steps. The assembly of the Gag to the PM, followed by budding and maturation. The details behind the mechanism of those processes are still unknown.

In this master thesis, the attachment and detachment of the major structural protein Gag was studied. Different cell lines were used to examine the Gag assembly. On one hand we used HeLa Kyoto cells where the assembly occurs stochastically, on the other hand HeLa Ad8Eg5.5 and HeLa Ad8E cells, where the assembly was synchronized using a rCDS. The transfected cells were measured via two different fluorescence-based methods, TIRF and RICS.

TIRF measurements were performed to observe Gag binding to the PM. The focus was laid on the kinetic behind these process and the question if Gag attaches as monomer or oligomer to the PM.

The results revealed that the assembly rate is in the range of $5 \cdot 10^{-3} \text{s}^{-1}$, which is in a good agreement with published values. This means that the particles bind in a short time range to the inner leaflet of the membrane. However, in which form the Gag arrives at the PM was not clearly assumed. The curve progression of the plotted traces suggest that most of the Gag attached as monomer, because most of the selected traces showed a continuous gradient. Otherwise, steps in the traces are evidence for the fact that Gag can also attach as oligomers to the PM. This means that the oligomerization took place earlier in the cytoplasm. In order to be able to make more precise statements, more cells would have to be measured to increase the statistics. Additionally there are also more analyzing methods to provide more informations about the details behind this mechanism.

As we were also interested in the detachment of Gag from the PM after adding rCD1, RICS measurements were performed. With this method it was possible to look directly at the Gag concentration in the cytoplasm. The calculated diffusion coefficients revealed that the mobility of the pCHIV.eGFP was around $6 \mu\text{m}^2/\text{s}$. The eGFP alone has a diffusion constant of $23 \mu\text{m}^2/\text{s}$. a higher mobility than the one bounded to Gag. This was expected because the eGFP is much smaller than the Gag, which means that it diffuses faster through the cytoplasm.

Beside the diffusion, the molecular brightness, mobile and immobile fraction was also determined. The results suggest that the mobile fraction decreases while the value of

the immobile species rises over the measurement time after addition of rCD1. This could potentially be explained by the fact that the Gag detaches as oligomer from the inner leaflet of the membrane. As a result it has a higher mass, which means that the diffusion constant is so slow that it apparently counts to the immobile fraction.

For a better understanding and to be able to make more precise assumptions about the assembly process, it is necessary to measure more cells to increase the statistics. The RICS measurements could be repeated with a protein inhibitor. The inhibitor would avoid new protein synthesis of Gag in the cytosol. This could change the results of the molecular brightness, mobile and immobile fraction. Additionally, different measurement conditions could also influence the results.

References

- [1] **W.I. Sundquist and H.G. Kräusslich.** HIV-1 Assembly, Budding, and Maturation. *Cold Spring Harb Perspect Med*, 2:a006924, 2012.
- [2] **F. Mücksch, V. Laketa, B. Müller, C. Schultz and H.G. Kräusslich.** Synchronized HIV assembly by tunable PIP₂ changes reveals PIP₂ requirement for stable Gag anchoring. *eLife*, 6:e25287, 2017.
- [3] **B. Meng and A.M.L. Lever.** Wrapping up the bad news – HIV assembly and release. *Retrovirology*, 10:5, 2013.
- [4] **L.A. Carlson, J.A. Briggs, B. Glass, J.D. Riches, M.N. Simon, M.C. Johnson, B. Müller, K. Grünwald and H.G. Kräusslich.** Three-dimensional analysis of budding sites and released virus suggests a revised model for HIV-1 and MLV Gag and facilitates their budding. *Mol Biol Cell*, 18:3193-3203, 2008.
- [5] **J. Hendrix, V. Baumgärtel, W. Schrimpf, S. Ivanchenko, M.A. Digman, E. Gratton, H.G. Kräusslich, B. Müller and D.C. Lamb.** Live-cell observation of cytosolic HIV-1 assembly onset reveals RNA-interacting Gag oligomers. *J.Cell.Biol.*, 4:629-646, 2015.
- [6] **A. Ono and E.O. Freed.** Plasma membrane rafts play a critical role in HIV-1 assembly and release. *Proc Natl Acad Sci*, 98: 13925-13930, 2001.
- [7] **S.B. Kutluay and P.D. Bieniasz.** Analysis of the initiating events in HIV-particle assembly and genome packaging. *PLoS Pathog*, 6:e1001200, 2010.
- [8] **N. Jouvenet, S.M. Simon and P.D. Bieniasz** Imaging the interaction of HIV-1 genomes and Gag during assembly of individual viral particles. *Proc Natl Acad Sci*, 106:19114-19119, 2009.
- [9] **S.F. Johnsen and A. Telesnitsky.** Retroviral RNA dimerization and packaging: The what, how, when, where and why. *PLoS Pathog*, 6, 2010.
- [10] **M.D. Moore and W.S. Hu.** HIV-1 RNA dimerization: It takes two to tango. *AIDS Rev*, 11:91-102, 2009.
- [11] **T. Jacks, M.D. Power, F.R. Masiarz, P.A. Luciw, P.J. Barr and H.E. Varmus.** Characterization of ribosomal frameshifting in HIV-1 gag-pol expression. *Nature*, 331:280-283, 1988.

- [12] **A.D. Frankel and J.A. Young.** HIV-1: Fifteen proteins and an RNA. *Annu Rev Biochem*, 67:1-25, 1998.
- [13] **E.O. Freed.** HIV-1 replication. *Somat Cell Molec Gen*, 26:13-33, 2001.
- [14] **A. Ono, S.D. Ablan, S.J. Lockett, K. Nagashima and E.O. Freed.** Phosphatidylinositol (4,5) bisphosphate regulates HIV-1 Gag targeting to the plasma membrane. *Proc Natl Acad Sci*, 101: 14889-14894, 2004.
- [15] **M. Lorizate and H.G. Kräusslich.** Role of lipids in virus replication. *Cold Spring Harbor Perspectives in Biology*, 3:a004820, 2011.
- [16] **E.O. Freed.** HIV-1 assembly, release and maturation. *Nature Reviews Microbiology*, 13:484-496, 2015.
- [17] **P. Spearman, R. Horton, L. Ratner and I. Kuli-Zade.** Membrane binding of human immunodeficiency virus typ 1 matrix protein in vivo supports a conformational myristoyl switch mechanism. *Journal of Virology*, 71:6582-6592, 1997.
- [18] **J.S. CLIP, J. Miller, J. Tai, A. Kim, R.H. Ghanam, and M.E. Summers.** Structural basis for targeting HIV-1 Gag proteins to the plasma membrane for virus assembly. *Proc Natl Acad Sci*, 103: 11364-11369, 2006.
- [19] **R.C. Aloia, F.C. Jensen, C.C. Curtain, P.W. Mobley and L.M. Gordon.** Lipid composition and fluidity of the human immunodeficiency virus. *Proc Natl Acad Sci*, 85:900-904, 1988.
- [20] **R.C. Aloia and F.C. Jensen.** Lipid composition and fluidity of the human immunodeficiency virus envelope and host cell plasma membranes. *Proc Natl Acad Sci*, 90:5181-5185, 1993.
- [21] **V. Chukkapalli, J. Inlora, G.C. Todd and A. Ono.** Evidence in support of RNA-mediated inhibition of phosphatidylserine-dependent HIV-1 gag membrane binding in cells. *Journal of Virology*, 87:1600-1605, 2013.
- [22] **S. Feng, V. Laketa, F. Stein, A. Rutkowska, A. MacNamara, s. Depner, U. Klingmüller, J. Saez-Rodriguez and C. Schultz.** A rapidly reversible chemical dimerizer system to study lipid signaling in living cells. *Angewandte Chemie Internationale Edition*, 53:6720-6723, 2014.
- [23] **J. Votteler and W.I. Sundquist.** Virus Budding and the ESCRT Pathway. *Cell Host and Microbe*, 14:232-241, 2013.

- [24] **J. Prescher, V. Baumgärtel, S. Ivanchenko, A. A. Torrano, C. Bräuchle, B. Müller and D. C. Lamb.** Super-Resolution Imaging of ESCRT-Proteins at HIV-1 Assembly sites. *PLOS Pathogens*, 10(2):e1004677, 2015.
- [25] **V. Baumgärtel, S. Ivanchenko, A. Dupont, M. Sergeev, P.W. Wiseman, H.G. Kräusslich, C. Bräuchle, B. Müller and D.C. Lamb.** Live-cell visualization of dynamics of HIV budding site interactions with an ESCRT component. *NATURE CELL BIOLOGY*, 13:4, 2011.
- [26] **S. Ghazi-Tabatabai, S. Saksena, J.M. Short, A.V. Pobbati, D.B. Veprintsev, R.A. Crowther, S.D. Emr, E.H. Egelman and R.L. Williams.** Structure and disassembly of filaments formed by the ESCRT-III subunit Vps24. *Structure*, 16:1345-1356, 2008.
- [27] **G. Fabrikant, S. Lata, J.D. Riches, J.A. Briggs, W. Weissenhorn and M.M. Kozlov.** Computational model of membrane fission catalyzed by ESCRT-III. *PLoS Comput Biol*, 5:e1000575, 2009.
- [28] **J.B. Cooper.** Aspartic proteinases in disease: A structural perspective. *Curr Drug Targets*, 3:155-173, 2002.
- [29] **H.T. McMahon and E. Boucrot.** Molecular mechanism and physiological functions of clathrin-mediated endocytosis. *Nat.Rev.Mol.Cell Biol.*, 12:517-533, 2011.
- [30] **S. Ivanchenko, W.J. Godinez, M. Lampe, H.G. Kräusslich, R. Eils, K. Rohr, C. Bräuchle, B. Müller and D.C. Lamb.** Dynamics of HIV-1 Assembly and Release. *PLoS Pathogens*, 5:e1000652, 2009.
- [31] **B.K. Ganser, S. Li, V.Y. Klishko, J.T. Finch and W.I. Sundquist.** Assembly and analysis of conical models for the HIV-1 core. *Science*, 283:80-83, 1999.
- [32] **M. Galilee, E. Britan-Rosich, S.L. Griner, R.M. Stroud, A. Marx and A. Alian.** The Preserved HTH-Docking Cleft of HIV-1 Integrase Is Functionally Critical. *Cell Press*, 24:1-11. 2016.
- [33] **H.G. Göttlinger, T. Dorfman, J.G. Sodroski and W.A. Haseltine.** Effect of mutations affecting the p6 gag protein on human immunodeficiency virus particle release. *Proc. Natl. Acad. Sci.*, 88:3195-3199, 1991.
- [34] **J.A. Briggs and H.G. Kräusslich.** The molecular architecture of HIV. *J.Mol.Biol.*, 410:491-500, 2011.

- [35] **E.R. Weiss and H. Göttliger.** The role of cellular factors in promoting HIV budding. *J.Mol.Biol*,410:525-533, 2011.
- [36] **V.Baumgärtel, B. Müller and D.C. Lamb.** Quantitative Live-Cell Imaging of Human Immunodeficiency Virus (HIV-1) Assembly. *Assembly. Viruses*, 4:777-799, 2012.
- [37] Lecture of **Prof. Lamb.** LMU: Fluorescence spectroscopy. winter semester 2016.
- [38] **H.H. Jaffe and A.L. Miller** *J.Chem.Educ.*, 43:469, 1966.
- [39] **A.L.P. Nery, R.M. Liegel and C. Fernandez.** Fluorescence and Chemiluminescence: Teaching Basic Principles by Simple Demonstration Experiments *CEJ*, 13:13-22, 2009.
- [40] **J. Wiedenmann, F. Oswald and G.U. Nienhaus.** Fluorescent proteins for live cell imaging: Opportunities, Limitations and challenges. *IUBMB Life*, 61:1029-1042, 2009.
- [41] **G. Zhang, V. Gurtu and S.R. Kain.** An enhanced green fluorescent protein allows sensitive detection of gene transfer in mammalian cells. *Biochem Biophys Res Commun*, 227(3):707-11, 1996.
- [42] **C.S. Colding-Christensen.** Fluorescence Microscopy – the Magic of Fluorophores and Filters. *BiteziseBio*, 2017.
- [43] **N.C. Shaner, R.E. Campbell, P.A. Steinbach, B.N.G. Giepmans, A.E. Palmer and R.Y. Tsien.** Improved monomeric red, orange and yellow fluorescent proteins derived from *Discosoma* sp. red fluorescent protein. *Nature Biotechnology*, 22:1567-1572, 2004.
- [44] **J.B. Grimm, B.P: English, J. Chen, J.P. Slaughter, Z. Zhang, A. Revyakin, R. Patel, J.J. Macklin, D. Normanno, R.H. Singer, T. Lionnet and L. D. Lavis.** A general method to improve fluorophores for live-cell and single-molecule microscopy. *Nature Methods*, 12:244-250, 2015.
- [45] **N. Jouvenet, P.D. Bieniasz and S.M. Simon.** Imaging the biogenesis of individual HIV-1 virions in live cells. *Nature*, 454:236-240, 2008.
- [46] **D.A. Woods and C.D: Bain.** Total internal reflection spectroscopy for studying soft matter. *The Royal Society of Chemistry*, 10:1071-1096, 2014.

- [47] **D.Axelrod.** Cell-Substrate Contacts Illuminated by Total Internal Reflection Fluorescence. *The Journal of Cell Biology*, 89:141-145, 1981.
- [48] **N.J. Harrick.** Internal reflection spectroscopy. *Wiley-Inter-science Div*, 1967.
- [49] **D.Axelrod.** Total Internal Reflection Fluorescence Microscopy in Cell Biology. *Traffic*, 2:764-774, 2001.
- [50] **V.M. Ingram.** A side view of moving fibroblasts. *Nature*, 222:641-643, 1969.
- [51] Lecture of **Prof.Hartschuh.** LMU: Microscopy for Nanotechnology. winter semester 2016.
- [52] **D.V: Buonomano** The biology of time across different scales. *Nat.Chem.Biol*, 3:594-97, 2007.
- [53] **D. Magde, E. Elson and W.W. Webb.** Thermodynamic fluctuations in a reacting system- measurement by fluorescence correlation spectroscopy. *Phys.Rev.Lett*, 29:705-708, 1972.
- [54] **K.M. Berland, P.T. So and E. Gratton.** Two-photon fluorescence correlation spectroscopy: method and application to the intracellular environment. *Biophys.J.*, 49:809-815, 1995.
- [55] **M.A. Digman, P. Sengupta, P.W. Wiseman, C.M. Brown, A.R. Horwitz and E. Gratton.** Fluctuation Correlation Spectroscopy with a Laser-Scanning Microscope: Exploiting the Hidden Time Structure. *Biophysical Society*, 10.1529:33-36, 2005.
- [56] **N. Bag and T. Wohland.** Imaging Fluorescence Fluctuation Spectroscopy: New Tools for Quantitative Bioimaging. *Annu. Rev. Phys. Chem*, 65:225-48, 2014.
- [57] **N.O. Petersen, P.L Hoddelius, P.W: Wiseman, O. Seger and K.E: Magnusson.** Quantitation of membrane receptor distributions by image correlation spectroscopy:concept and application. *Biophys. J.*, 65:1135-1146, 1993.
- [58] **B. Zhang, J. Zerubia and J.C: Olivo-Marin.** Gaussian approximations of fluorescence microscope point spread function models. *Appl. Opt.*, 46:1819-1896, 2007.
- [59] **E. Keating, A. Nohe and N.O Petersen.** Studies of distributaion, location and dynamic properties of EGFR on the cell surface measured by image correlation spectroscopy. *Eur. Biophys. J.*, 37:469-481, 2008.

- [60] **P.W. Wiseman, J.A. Squier, M.H. Ellisman and K.R. Wilson.** Two-photon video rate image correlation spectroscopy (ICS) and image cross-correlation spectroscopy (ICCS). *J. Microsc.*, 200:14-25, 2000.
- [61] **P.W. Wiseman, C.M. Brown, D.J. Webb, B. Herbert, N.L. Johnson, J.A. Squier, M.H. Ellisman and A.F. Horwitz.** Spatial mapping of integrin interaction and dynamics during cell migration by image correlation spectroscopy. *J. Cell Sci.*, 117:5521-5534, 2004.
- [62] **N.O. Petersen.** Scanning fluorescence spectroscopy. I. Theory and simulation of aggregation measurements. *Biophys. J.*, 49:809-815, 1986.
- [63] **D.L. Kolin and P.W. Wiseman.** Advances in Image Correlation Spectroscopy: Measuring Number Densities, Aggregation States, and Dynamics of Fluorescently labeled Macromolecules in Cells. *Cell Biochem. Biophys.*, 49:141-164, 2007.
- [64] **C.M. Brown, R.B. Dalal, B. Hebert, M.A. Digman, A.R. Horwitz and E. Gratton.** Raster image correlation spectroscopy (RICS) for measuring fast protein dynamics and concentrations with a commercial laser scanning confocal microscope. *J. Microsc.*, 229(01):78-91, 2008.
- [65] **M.A. Digman, C.M. Brown, P. Sengupta, P.W. Wiseman, A.R. Horwitz and E. Gratton.** Measuring fast dynamics in solutions and cells with a laser scanning microscope. *Biophysical journal*, 89:1317-1327, 2005.
- [66] **B. Münch, P. Trtik, F. Marone and M. Stampanoni.** Stripe and ring artifact removal with combined wavelet-Fourier filtering. *OPTICS EXPRESS*, 17:10:8567-8590, 2009.
- [67] **B. Müller, E. Zaychikov, C. Bräuchle and D.C. Lamb.** Pulsed Interleaved Excitation. *Biophys. J.*, 89:3508-3522, 2005.
- [68] **A.N. Kapanidis, N.K. Lee, T.A. Laurence, S. Doose, E. Margeat and S. Weiss.** Fluorescence-aided molecule sorting: analysis of structure and interactions by alternating-laser excitation of single molecules. *Proc. Natl. Acad. Sci.*, 101:8936-8941, 2004.
- [69] **S. Mallat** A Wavelet Tour of Signal Processing. *Academic Press.*, 2. Edition, 1999.
- [70] **M. Holschneider, R. Kronland-Martinet and J. Morlet.** A real-time algorithm for signal analysis with the help of the wavelet transform. *Springer*, 286-297, 1989.

- [71] **J.C. Olivo-Marin.** Extraction of spots in biological images using multiscale products. *Pattern Recognition*, 35:1989-1996, 2002.
- [72] **Q. Ruan, Y.Chen, E.Gratton, M. Glaser and W.W.Mantulin.** Cellular characterization of adenylate kinase and its isoform: two-photon excitation fluorescence imaging and fluorescence correlation-spectroscopy. *Biophys.J.*, 83:3177-3187, 2002.
- [73] **U. Haupts, S. Maiti, P. Schwille and W.W. Webb.** Dynamics of fluorescence fluctuations in green fluorescent protein observed by fluorescence correlation spectroscopy. *Proc.Natl.Acad.Sci.*, 95:13573-13578, 1998.
- [74] **D.R. Larson, Y.M. Ma, V.M. Vogt and W.W.Webb.** Direct measurement of Gag-Gag interactions during retrovirus assembly with FRET and fluorescence correlation spectroscopy. *J.Cell Biol.*, 162:1233-1244, 2003.
- [75] **J. Hendrix, T. Dekens, W. Schimpf and D.C. Lamb.** Arbitrary-Region Raster Image Correlation Spectroscopy. *Biophysical.J.*, 111:1785-1796, 2016.

List of Figures

1	Schematic representation of Gag. The protein consists of four domains, the matrix domain (MA), the capsid domain(CA), a nucleocapsid domain (NC) and a P6 domain as well as the two spacer peptides SP1 and SP2 and . The cleavage sites are shown in black arrows. ^[1]	3
2	Gag MA domain (yellow) anchoring to the inner leaflet of the PM (gray) via myristoyl switch. The aliphatic myristoyl group (brown) and the basic residues on the membrane binding surface of the MA surface (blue) interact with the PIP_2 (red). ^[18]	4
3	Schematic illustration of the principle of the reversible chemical dimerizer system for controlling PIP_2 concentration. The anchor is shown in blue and in red the enzyme phosphatase localized at the inner leaflet of the PM. Under normal PIP_2 concentration the Gag can bind to the inner leaflet of the PM, by adding rCD1 (green) the concentration of phosphatase at the PM increases, which causes a conversion from PIP_2 to PIP. No Gag can bind to the PM unless FK506 (blue) is added. This causes the displacement of the enzyme from the PM, which restores PIP_2 levels rapidly. ^[2]	5
4	Development of the HIV-1, from infection to maturation. In (A) the integration of the proviral DNA into the host chromosome occurs followed by (B) the transcription and transport of the mRNA out of the nucleus and finally (C) the virus morphogenesis takes place. ^[1]	6
5	Illustration of the three stages of virion development. The viral genetic material is depicted in green-gray, Gag in colored blocks and the envelope glycoprotein in blue. ^[3]	7
6	Jablonski diagram, which shows possible energy transitions and mechanism. In blue the absorption of an electron from the energetic ground sate (S_0) to the excited state (S_1 or S_2) is presented. Green illustrates the fluorescence mechanism and in red the phosphorescence is pictured. ^[39] . . .	10
7	(A)Crystal structure of the green fluorescent protein and (B) the spectra of the excitation (blue) and emission (red). ^[41]	11
8	(A) Crystal structure and (B) the excitation (blue) and emission (red) spectra of a monomeric red fluorescent protein. ^[43]	12
9	(A) The structure and (B) the excitation emission spectra of the red fluorescence dye JF646 as NHS-coupled derivative. ^[44]	12
10	(A) Chemical structural formula and (B) the excitation and emission spectra of the yellow fluorescence dye JF549. ^[44]	13
11	Schematic representation of the total internal reflection fluorescence principle. The laser beam reaches the glass slide at the critical angle θ_c , which leads to the excitation (red) of the fluorophores (green) near the interface by creating an evanescent wave. ^[46]	14

12	Illustrations of the beam path in (A) the case that the refractive indexes of glass and immersion medium are the same and in (B) that the reflection index is smaller than the one from glass, for example air(1.0). ^[51]	15
13	Image recording with a CLSM for RICS. The scanning of the sample occurs in sawtooth pattern by a laser beam. The timescale in scan direction is in the microsecond (blue) range, while between two lines in an image it is in the millisecond (red) range and between frames in seconds (purple). ^[56]	18
14	2D-plot of a calculated spatial autocorrelation function (SACF). The concentration can be determined by the amplitude, while the diffusion over the shape of the decay. ^[56]	19
15	2D-plots of RICS measurement dependent on the diffusion coefficient. SACF of molecules with (A) a fast diffusion constant and (B) of a slow diffusion constant. ^[56]	20
16	Picture of the wavelet decomposition, filtering the frequency through (a) a high pass and a low pass function followed by (c) downsampling. function ^[66]	21
17	The excitation (yellow) and emission (purple) of eGFP and mRFP (blue/red). In addition the excitation wavelength of eGFP (blue dashed line) and mRFP (orange dashed line). It is nicely represented that the respective emission is in the range of the used filter (black box).	27
18	The results of the tracking program. The image series is loaded and with setting the red box, the region is selected where the tracking should be done. The green dots represent spots which are tracked over longer frames and in blue those over less than four frames.	29
19	Decays of the signal of the blue and the yellow channel in PAM. The ranges of the yellow channel were set based on the signal delay, which means by separating the signal after yellow excitation of the cross talk after blue excitation.	30
20	Scan of Ad8E cells in purple and the transfected cells are shown in green.	32
21	Scan of the Ad8E cells (purple) transfected with pCHIV.eGFP (green).	33
22	Time course of a transfected Ad8E cell, showing the increase of HIV-particles (white) at the PM during the measurement.	34
23	The first and the last frame of a measured transfected Hela Kyoto cell were no new particle arrived at the PM.	34
24	Images of a shrinking Hela Kyoto cell.	35
25	Two different kinds of traces, the continuous rise of the countrate (A) and a "jump" in the trace (B).	36
26	The normalized plots of (A) a continuous trace and (B) a "jump" in the trace. The measurements were started, when 100 nM FK506 was added.	38
27	Plot of the normalized intensity against the time for all tracked particles (A), and for only the selected particles (B). The start point of each intensity trace is the first time when the particle was tracked.	39

28	Diagrams of the determined average assembly rate and the assembly rate of the selected particles of (A) HeLa Kyoto cells, and in (B) of Ad8E cells.	40
29	Images of an Ad8E cell after the addition of 100 nM rCD1. The measurements were performed at 37 °C and 5% CO ₂ recorded with an exposure time of 50 ms and an interframe time of 500 ms.	41
30	Diagram of the normalized intensity of all tracked particles against the time for an Ad8E cell after adding 100 nM rCD1.	41
31	The diffusion coefficient of all measured Ad8E and Ad8Eg5.5 cells transfected with pCHIV.eGFP plotted as a whisker-plot with standard variation. The values of each cells are given in red circles.	43
32	The spatial autocorrelation of pCHIV.eGFP, where ξ and ψ are the spatial lag time in the x and y direction. In (A) the 2D plot of the spatial correlation function is shown and in (B) the fitted correlation with a color-coded goodness-of fit. Gray illustrates a good fit, while red and blue regions indicates higher residuals.	43
33	The normalized average results of all measured cells were plotted together as barplot with errorbars. In (A) the time is plotted against the relative molecular brightness, in (B) against the number of the mobile fraction and in (C) against the number of the immobile components. All measurements were started at point 0. In the cases of pCHIV.eGFP and pCHIV.CLIP with the addition of rCD1.	46
34	Results of measured pCHIV.eGFP transfected cells, after the addition of 100 nM rCD1. The plots were generated from 25 out of 28 measured cells. In (A) the time is plotted against the molecular brightness, in (B) against the mobile species and in (C) against the immobile components.	64
35	Diagrams of the control measurements, started after the addition of 100 nM rCD1, of pCHIV.eGFP transfected cells. 6 out of 7 measured cells were used for the plots. In (A) the time is plotted against the brightness, in (B) against the mobile fraction and in (C) against the immobile species.	65
36	Diagrams of the pCHIV.CLIP measurements, started after the addition of 100 nM rCD1. In (A) the time is plotted against the brightness, in (B) against the mobile fraction and in (C) against the immobile species.	66

List of Tables

1	Utilized reagents	22
2	Transfection mixture.	24
3	Statistic of measured Hela Kyoto and Ad8E cells.	35
4	Statistic of the measured cells, were only XTremeGene 9 was used as transfection reagent.	35
5	Statistics of selected particles for different cell lines.	36
6	Determined average intensity of eGFP ₁ , eGFP ₅ and eGFP.GPI.	37
7	Diffusion coefficient of eGFP, eGFP dimer and eGFP tandem trimer at 37 °C.	42
8	Diffusion coefficient of the pCHIV.CIIP induced cells with differnt dyes.	44
9	Determined assembly rate of the analyzed Hela Kyoto cells.	61
10	Kinetic of the measured Ad8E cells.	62
11	Determined diffusion coefficient of the pCHIV.eGFP induced cells	63

Supplement

The determined assembly rate of the analyzed HeLa Kyoto and Ad8E cells are given in the following two tables. The plots of **Figure 28** were generated out of this results

Table 9: Determined assembly rate of the analyzed HeLa Kyoto cells.

Date	Sample Name	Average Assembly Rate [s⁻¹]	Assembly Rate only selected particles [s⁻¹]
06.04.2018	HeLa_pCHIV.eGFP_100_1.0_green	0.0456	0.0017
06.04.2018	HeLa_pCHIV-eGFP_100_1.0_green	0.0269	0.0012
17.04.2018	HeLa_pCHIV.eGFP_100_green	0.0844	0.0044
17.04.2018	HeLa_pCHIV.eGFP_100_green_3	0.0760	0.0011
27.04.2018	HeLa_pCHIV.eGFP_100_green_1	0.0339	0.0015
08.05.2018	HeLa_pCHIV.eGFP_100_green_1	0.0991	0.0082
06.04.2018	HeLa_pCHIV.eGFP_100_green_2	0.0352	0.0061
17.04.2018	HeLa_pCHIV.eGFP_100_green_4_5	0.0552	0.0081
17.04.2018	HeLa_pCHIV.eGFP_100_green_6	0.0646	0.0082
17.04.2018	HeLa_pCHIV.eGFP_100_green_7	0.0941	0.0096
17.05.2018	HeLa_pCHIV.eGFP_green_1	0.0596	0.0092
17.05.2018	HeLa_pCHIV.eGFP_green_2	0.0370	0.0033
17.05.2018	HeLa_pCHIV.eGFP_green_3	0.0553	0.0059
17.05.2018	HeLa_pCHIV.eGFP_green_4	0.0828	0.0037
	Average	0.0607 ± 0.0195	0.0052 ± 0.0027

Table 10: Kinetic of the measured Ad8Eg5.5 cells.

Date	Sample Name	Average Assembly Rate [s⁻¹]	Assembly Rate only selected particles [s⁻¹]
13.04.2018	Ad8Eg5.5_pCHIV.eGFP_green_2	0.0239	0.0011
17.04.2018	Ad8Eg5.5_pCHIV-eGFP_1.0_green	0.0090	0.0012
17.04.2018	Ad8Eg5.5_pCHIV.eGFP_green	0.0148	0.0018
18.04.2018	Ad8Eg5.5_pCHIV.eGFP_2_green	0.0844	0.0074
18.04.2018	Ad8Eg5.5_pCHIV.eGFP_green_1	0.0425	0.0033
25.04.2018	Ad8Eg5.5_pCHIV.eGFP_green_01	0.0331	0.0051
25.04.2018	Ad8Eg5.5_pCHIV.eGFP_green_1	0.0461	0.0057
25.04.2018	Ad8Eg5.5_pCHIV.eGFP_green	0.0389	0.0052
26.04.2018	Ad8Eg5.5_pCHIV.eGFP_green_1	0.03606	0.0088
26.04.2018	Ad8Eg5.5_pCHIV.eGFP_green_2	0.0245	0.0092
27.04.2018	Ad8Eg5.5_pCHIV.eGFP_green	0.0373	0.0019
27.04.2018	Ad8Eg5.5_pCHIV.eGFP_green_1_2	0.0159	0.0022
04.05.2018	Ad8Eg5.5_pCHIV.eGFP_green_1	0.0809	0.0082
04.05.2018	Ad8Eg5.5_pCHIV.eGFP_green_3	0.0583	0.0026
09.05.2018	Ad8Eg5.5_pCHIV.eGFP_green	0.0993	0.0055
09.04.2018	Ad8Eg5.5_pCHIV.eGFP_green_1	0.0396	0.0069
09.05.2018	Ad8Eg5.5_pCHIV.eGFP_green_2	0.0337	0.0068
09.05.2018	Ad8Eg5.5_pCHIV.eGFP_green_3	0.0839	0.0063
16.05.2018	Ad8Eg5.5_pCHIV.eGFP_green_3	0.0558	0.0094
18.05.2018	Ad8Eg5.5_pCHIV.eGFP_green_1	0.0188	0.0082
18.05.2018	Ad8Eg5.5_pCHIV.eGFP_green_3	0.0191	0.0054
06.06.2018	Ad8Eg5.5_pCHIV.eGFP_green_6	0.0842	0.0073
	Average	0.0442 ± 0.0217	0.0053 ± 0.0022

In the next table the calculated diffusion coefficient of the pCHIV.eGFP induced cells are given, which were plotted in **Figure 31**.

Table 11: Determined diffusion coefficient of the pCHIV.eGFP induced cells

Date	Cell	average D [$\mu\text{m}^2/\text{s}$]
28.06.2018	1	6.51 ± 3.54
28.06.2018	2	4.97 ± 1.93
29.06.2018	1	3.20 ± 0.41
29.06.2018	2	3.37 ± 1.39
29.06.2018	3	2.40 ± 1.07
23.08.2018	1	5.41 ± 1.61
23.08.2018	2	15.2 ± 2.94
23.08.2018	3	3.46 ± 2.59
29.06.2018	4	7.99 ± 2.38
23.08.2018	5	9.26 ± 2.61
23.08.2018	6	10.52 ± 2.93
24.08.2018	1	3.79 ± 1.54
24.0.2018	2	3.87 ± 1.58
24.08.2018	3	6.06 ± 2.88
24.08.2018	4	4.16 ± 1.23
24.08.2018	5	9.30 ± 4.11
24.08.2018	6	7.23 ± 1.80
30.08.2018	1	4.53 ± 2.28
30.08.2018	2	7.37 ± 2.67
30.08.2018	3	3.80 ± 1.69
31.08.2018	1	7.53 ± 5.38
31.08.2018	2	3.63 ± 1.54
31.08.2018	3	2.77 ± 0.94
31.08.2018	4	4.36 ± 0.44
31.08.2018	5	5.75 ± 1.87
	Average	5.66 ± 2.13

In the following, the individual diagrams of brightness, mobile fraction and immobile fraction plotted against the time for each case of the RICS measurement are given.

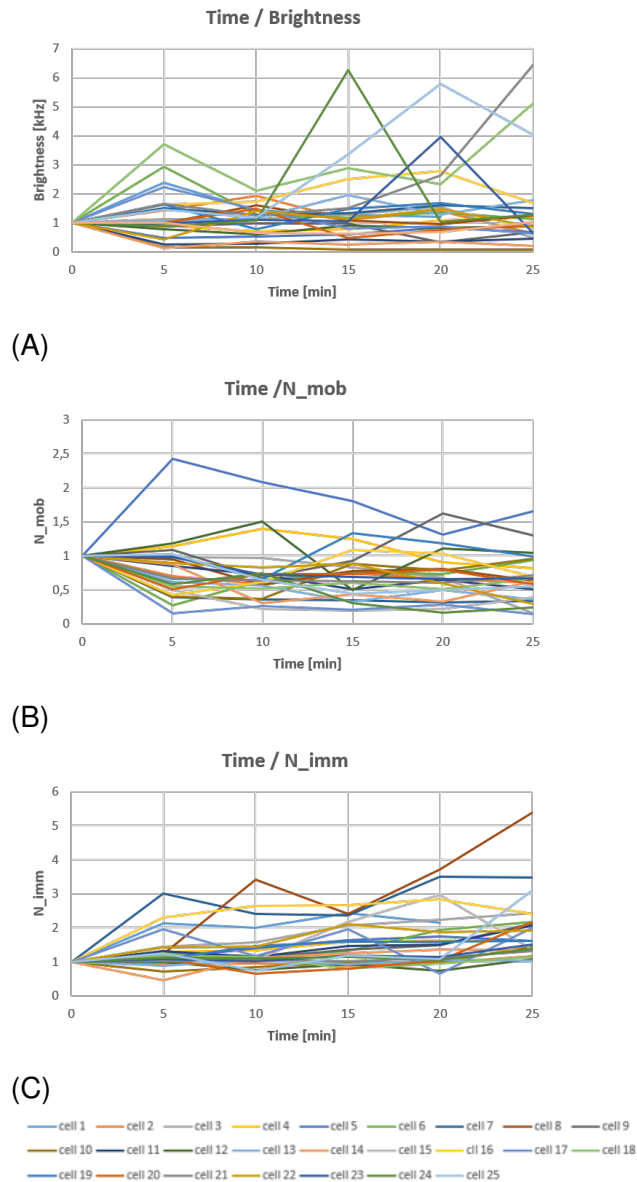


Figure 34: Results of measured pCHIV.eGFP transfected cells, after the addition of 100 nM rCD1. The plots were generated from 25 out of 28 measured cells. In (A) the time is plotted against the molecular brightness, in (B) against the mobile species and in (C) against the immobile components.

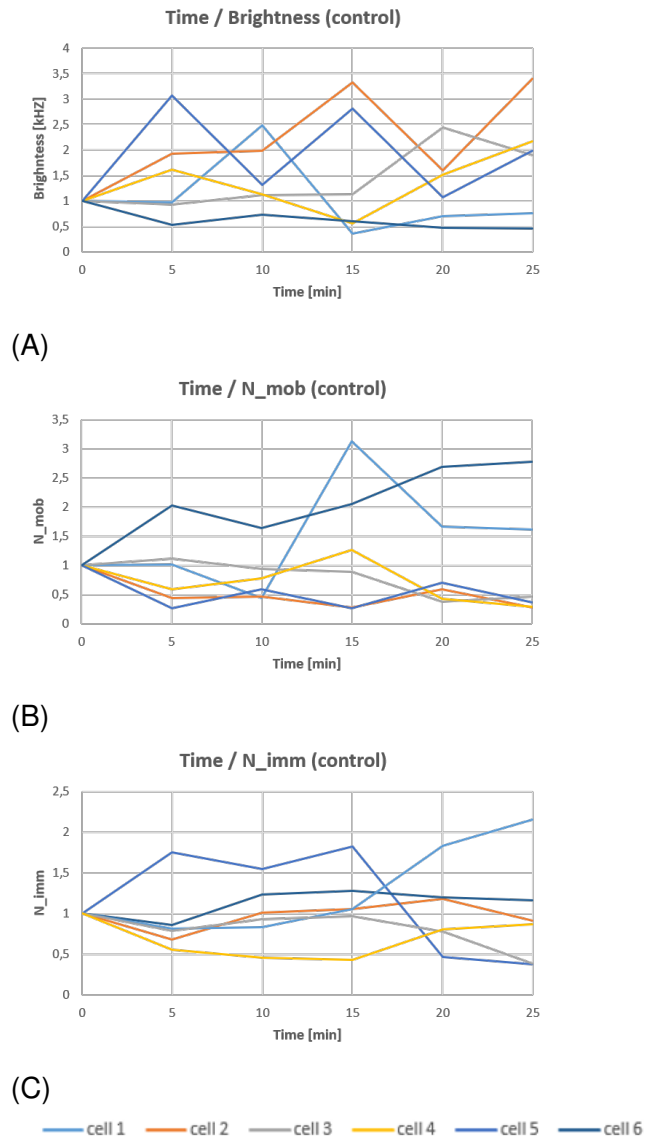


Figure 35: Diagrams of the control measurements, started after the addition of 100 nM rCD1, of pCHIV.eGFP transfected cells. 6 out of 7 measured cells were used for the plots. In (A) the time is plotted against the brightness, in (B) against the mobile fraction and in (C) against the immobile species.

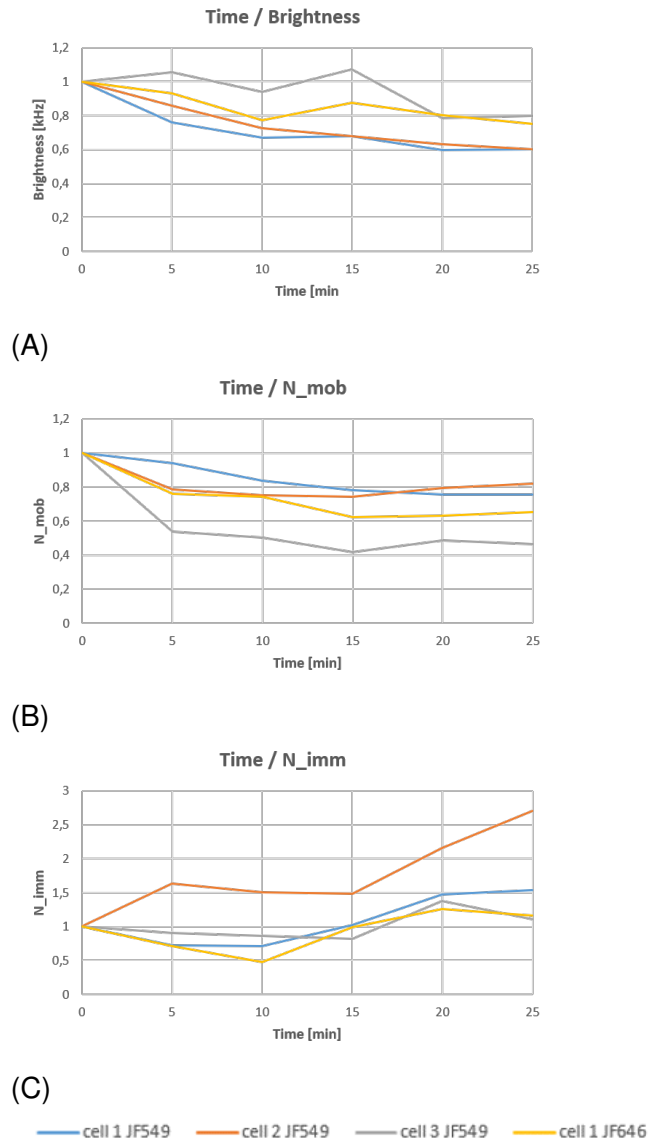


Figure 36: Diagrams of the pCHIV.CLIP measurements, started after the addition of 100 nM rCD1. In (A) the time is plotted against the brightness, in (B) against the mobile fraction and in (C) against the immobile species.